Genetic relationship between hydrocarbon system evolution and Carlin-type gold mineralization: Insights from Re-Os pyrobitumen and pyrite geochronology in the Nanpanjiang Basin, South China

Xiang Ge[1], David Selby[2,3], Junjie Liu[2,4], Youzhi Chen[5], Guofan Cheng[5], Chuanbo Shen[1*]

[1] Key Laboratory of Tectonics and Petroleum Resources, China University of Geosciences, Ministry of Education, Wuhan, 430074, China

[2] Department of Earth Sciences, Durham University, Durham DH1 3LE, UK

[3] State Key Laboratory of Geological Processes and Mineral Resources, China University of Geosciences, Wuhan 430074, China

[4] State Key Laboratory of Isotope Geochemistry, Guangzhou Institute of Geochemistry, Chinese Academy of Sciences, Guangzhou, 510640, China

[5] School of Resources and Environmental Engineering，Guizhou Institute of Technology，Guiyang 550003, China

Corresponding Author:

Professor Dr. Chuanbo Shen (Shen, C.B.)

Postal address: Key Laboratory of Tectonics and Petroleum Resources, China University of Geosciences, Ministry of Education, Wuhan, 430074, China

E-mail: cbshen@cug.edu.cn, cugshen@126.com

Tel.: +86-27-67883067; Fax. +86-27-67883051

ABSTRACT

The spatial association of hydrocarbons with metalliferous ore deposits is found worldwide and is particularly common to Carlin-type gold systems. Both liquid oil and pyrobitumen are found in Carlin-type gold deposits of North Nevada, USA and the Nanpanjiang Basin, South China. However, the temporal and genetic association of hydrocarbons and gold mineralization are still debated. To this end, using rhenium-osmium (Re-Os) geochronology of pyrobitumen and gold-bearing pyrite from the Laizishan and Banqi reservoirs and the Yata Carlin-type gold deposit in the Nanpanjiang Basin, we consider hydrocarbons played a critical role in the mineralization process.

A Re-Os age of 228 ± 16 Ma obtained for highly mature pyrobitumen suggests that liquid oil cracking occurred during the Late Triassic in the Laizishan and Banqi reservoirs. This age is in agreement with the modelled thermal history of the Nanpanjiang Basin. Additionally, a broadly identical gold-bearing pyrite Re-Os age of 218 ± 25 Ma from Yata Carlin-type gold deposit which is in agreement with ages reported for other Carlin-type gold deposits in the Nanpanjiang Basin (e.g., in-situ SIMS U-Pb rutile = 213.6 ± 5.4 Ma, Re-Os arsenopyrite = 204 ± 19 Ma - 235 ± 33 Ma and Rb-Sr illite = 212.8 ± 4.6 Ma) suggests the auriferous Carlin-type systems of the Nanpanjiang Basin also formed during the Late Triassic. Integrating our Re-Os data, with recent liquid hydrocarbon experimental data and fluid inclusion data from both reservoirs and gold deposits within the Nanpanjiang Basin, a methane (CH_4) dominated thermochemical sulfate reduction (TSR) process, which introduced

hydrogen sulfide (H_2S) into basinal fluid and ultimately led to the deposition of gold-bearing pyrite by sulfidation, is considered to be the genetic link between of pyrobitumen and gold-bearing pyrite mineralization of the Carlin-type systems of the Nanpanjiang Basin.

Key words:

Re-Os geochronology; pyrobitumen; pyrite; Carlin-type gold deposit; Nanpanjiang Basin; South China

1. INTRODUCTION

Sedimentary basins host key source units for both hydrocarbon and metal resources (Parnell, 1994; Liu et al., 2000). In many cases, both a temporal and spatial relationship exists between hydrocarbon migration/accumulation and the formation of mineral systems, such as Mississippi Valley-type (MVT) lead-zinc deposits in the Midcontinent, USA, and Nunavut, Canada (Anderson, 1975; Kesler et al., 1994; Selby et al., 2005; Saintilan et al., 2019), sandstone uranium deposits in the ChuSarysu and Syrdarya basins in Kazakhstan (Jaireth et al., 2008), and vein-type uranium deposits in Czech Republic (Kribek et al., 1999). Hydrocarbons (oil, bitumen or pyrobitumen) are also associated with gold systems worldwide, for example gold-uranium deposits in the Witwatersrand Basin, South Africa (Robb and Meyer, 1995; Fuchs et al., 2016), the Owen Lake epithermal Ag-Au vein deposit, central British Columbia (Thomson et al., 1992), orogenic gold deposits both in Cosmo Howley, Northern territories, Australia and West Qinling, China (Mirasol-Robert et al., 2017; Xiong et al., 2019; Wu et al., 2020) and Carlin-type gold deposits in the Alligator Ridge district, Nevada, USA (Hulen et al., 1998; Hulen and Collister, 1999; Muntean, 2018a). Carlin-type gold deposits (micro-disseminated gold commonly hosted in hydrothermal pyrite ± arsenopyrite) are a hydrothermal deposit type occurring in certain types of sedimentary basins (Hofstra and Cline, 2000). Differences between the Carlin-style deposits in Nevada and other similar deposits worldwide have led to a proliferation of terms, including Carlin-type, Carlin-like, sedimentary rock-hosted and distal disseminated, gold deposits. Characteristics including tectonic setting, host rocks, gold occurrence, hydrothermal alteration, and ore paragenesis were used to define those types of gold deposits (Muntean, 2018b). Comparison of the gold deposits in Nevada and the Nanpanjiang Basin, South China, show that both groups of deposits have, (1) a similar tectonic evolution; (2) invisible gold residing in fine-grained (<10 µm) pyrite or within pyrite rims on gold-poor pyrite cores (Su et al., 2012; Cline, 2018; Yan et al., 2018); (3) host rocks consisting of limestone and/or calcareous siltstone; and (4) alteration assemblages that reflect sulfidation, decarbonatization, silicification, and argillization processes (Xie et al., 2018a). These similarities, notwithstanding some differences including ore-stage pyrite morphology, wall rock alteration, CO_2 abundance in the ore fluids (Xie et al., 2018a), suggest that the gold deposits in the Nanpanjiang Basin belong to the Carlin-type classification (Muntean, 2018b). The Carlin-type gold deposits of the Nanpanjiang Basin, with an estimated reserve of more than 700 tonnes of Au, make the region the second largest in the world after Nevada (Jin et al., 2016; Muntean, 2018a; Su et al., 2018).

Similar to the Carlin-type gold deposits in Alligator Ridge district, Nevada (Hulen and Collister, 1999; Nutt and Hofstra, 2003), hydrocarbon, especially pyrobitumen, is spatially related to the gold deposits in the Nanpanjiang Basin (Gu et al., 2010; Tan et al., 2015; Liu et al., 2016) (Fig. 1). However, any role of hydrocarbons in the formation gold deposits is debated. For example, the similar organic gas (e.g., CH_4, C_2H_6) component within fluid inclusions from different mineralization stages (Jin et al., 2016) has been used to suggest there is no genetic relationship between hydrocarbons and gold mineralization, with its spatial association being only coincidental. In contrast, it has been suggested that hydrocarbons can be enriched metals. For example, Au, Zn, and U, with Au reaching ppm levels (Large et al., 2011; Migdisov et al., 2017). The source of Au in Carlin-type gold systems is also debated, with both metal-enriched sedimentary formations (Hofstra and Cline, 2000; Emsbo et al., 2003; Large et al., 2011) and magmatic-hydrothermal activity (Muntean et al., 2011; Large et al., 2016; Zhu et al., 2020) being consider as the progenitor. In both cases Au bearing fluids can interact with liquid oil in the shallow crust (Fetter et al., 2019). Yet, the lack of coeval igneous intrusions near the gold deposits of the Nanpanjiang Basin, as well as elevated $\delta^{34}S$ values of ore-related sulfide minerals (Xie et al., 2018b) are interpreted to indicate basinal derived fluids could have played an important role during mineralization (Gu et al., 2012). The apparent association of gold and organic matter in the Witwatersrand Basin, South Africa (Parnell and

McCready, 2000), the Erickson gold mine, northern British Columbia, Canada (Mastalerz et al., 1995), gold-bearing bitumen in gold deposits at Elliot Lake-Blind River region of Ontario, Canada (Mossman et al., 1993) and Cherry Hill, California (Pearcy and Burruss, 1993) suggest hydrocarbon fluids have entrained gold during migration or entrapped gold from the parent fluid and then promote gold precipitation as a reductant. Additionally, recent experimental data show that oil could either aid gold pre-enrichment or act as the metal carrier before metal precipitation (Zhuang et al., 1998; Migdisov et al., 2017; Crede et al., 2019).

Rhenium and Os are both siderophilic and chalcophilic and commonly are enriched in metal sulfides (e.g., pyrite). The Re-Os radioisotope system has been proven to be a robust tool for determining the timing and duration of sulfide and cogenetic ore mineralization (e.g., Stein et al., 2000; Selby et al., 2009; Hnatyshin et al., 2020). Additionally, Re and Os are also organophilic, and are typically enriched in hydrocarbons (oil, bitumen, pyrobitumen), with the Re-Os isotope systematics recording the timing of liquid oil, pyrobitumen formation, and by inference dry-gas generation (e.g., Selby and Creaser, 2005; Ge et al., 2016; Georgiev et al., 2016; Liu and Selby, 2017; Liu et al., 2018; Georgiev et al., 2019). In order to resolve the spatial relationship between pyrobitumen and Carlin-type gold in the Nanpanjiang Basin, the Laizishan and Banqi paleo-reservoirs and Yata Carlin-type gold deposit were chosen for Re-Os dating of pyrobitumen and gold-bearing pyrite. Integrating our data with previous studies (e.g., petrography, isotope dating, basin modeling, fluid inclusion analysis), the new Re-Os data aid in providing the direct timing of reservoir evolution, as well as the age of the Carlin-type gold mineralization, and yield insights into the genetic relationship between hydrocarbons and gold mineralization.

2. GEOLOGICAL SETTING

The Nanpanjiang Basin, located at the junction of Guizhou, Yunnan, and Guangxi provinces, occurs within the southwest margin of the South China block (Fig. 1A) (Liu et al., 2016; Yan et al., 2018). The total area of the basin is ~90,000 km^2 and is fault-bounded by the Indochina block, Kangdian area, Jiangnan orogenic belt, and the Qinfang fold belt (Fig. 1A, B) (Liu et al., 2016). The Nanpanjiang Basin records a complex tectonic evolution since the early Paleozoic. Beginning with the formation of the South China block during the Caledonian orogeny (Liu et al., 2001), this region evolved from a rifted basin during the Devonian to a passive continental margin from the early Carboniferous to the early Triassic, the latter controlled by the Hercynian orogeny (Qin et al., 1996; Du et al., 2013; Lai et al., 2014). Associated with the opening of the Ailaoshan Ocean and northward motion of the South China block, northeast-southwest extension resulted in the formation of the Nanpanjiang Basin during the Devonian (Qin et al., 1996; Du et al., 2013). With the closure of the Tethys Ocean and the subduction of Ailaoshan orogenic belt, the Indosinian terrane collided with the South China block during the Middle Triassic (Indosinian orogeny), which led to collision of the Nanpanjiang Basin with the North Vietnam block (Qin et al., 1996; Zaw et al., 2014). Following the Indosinian orogeny, the late Triassic-early Jurassic Yanshanian orogeny resulted in intracontinental deformation of the Nanpanjiang basin (Cai and Zhang, 2009; Zaw et al., 2014).

Precambrian to very Early Devonian strata are mostly absent in the Nanpanjiang Basin (Liu et al., 2016). However, the late early Devonian to middle Triassic is well preserved (Du et al., 2013; Liu et al., 2016). Devonian strata mainly consist of sandstone, siltstone, shale, and marlstone with a total thickness of ca. 400 m (Liu et al., 2016). The Carboniferous to Permian is represented by 3000 m of shallow-water platform carbonate in the northwest, and by a deep-water basinal sequence with some shallow water carbonate platforms in the southeast (Fig. 1). The two depositional systems are separated by the Poping thrust fault (F6) (Du et al., 2013). The carbonate platforms mainly consist of bioreef limestone, micrite, and oolitic limestone and breccia, with the basin facies composed of siliceous- and clay-rich units and black mudstone (Liu et al., 2016) (Fig. 2). Some of the Permian strata (Permian Maokou Formation) comprises up to 500 m of pyroclastic rocks related to ~260 Ma Emeishan volcanism (Jin et al., 2016). The Triassic is represented by 6000 m of clastic turbidites that consist of mixed sandstone and mudstone (Liu et al., 2016).

Shales and mudstones occur throughout the Devonian to Triassic strata within the Nanpanjiang Basin. Geological survey and geochemical analysis on the potential source rocks found that the Devonian shales of ~2000m thickness, with an organic carbon abundance (TOC) > 1.5 %, are the major hydrocarbon source rock within the basin (Zhao et al., 2006c). Whereas, the Permian to Triassic marlstones and calcareous shale which possess very low TOC (<0.5 %) coupled with a limited distribution have a very poor hydrocarbon generation capacity (Zhao et al., 2006c). The Middle to Late Permian limestone (reef limestone and platform carbonate) are the key paleo-reservoir units, with hydrocarbon shows mainly observed in vugs and on fracture planes (Zhao et al., 2007). In the Laizishan and Banqi domes, solid bitumen is found within vugs and/or along fractures in the Late Permian Wujiaping Formation (Fig. 3). The solid bitumen in the Late Permian Wujiaping Formation is characterized by being insoluble in organic solvents (e.g., carbon disulfide, chloroform), having low H/C ratios (0.17-0.52) and high bitumen reflectance (e.g., BRo % >2.0 %)(Zhao et al., 2007), indicating the bitumen exhibits a high hydrocarbon maturity and is pyrobitumen (Zhuang et al., 2000; Zhao et al., 2007).

Carlin-type gold deposits in the Nanpanjiang Basin are mainly found in the Permian to Triassic carbonate and terrigenous clastic units (Su et al., 2018). The deposits are classified as Stratabound Type, Fault Type, and Compound Type (Gu et al., 2013; Jin et al., 2016). The Stratabound Type gold deposits (Shuiyindong, Nibao, Getang) are distributed within carbonate platform facies and are closely associated with a detachment fault or the regional unconformity between the Permian Maokou and Longtan formations; the Fault Type deposits (Lannigou, Yata, Banqi, Zhesang) are within the basin center and are spatially associated with high-angle thrust faults; the Compound Type deposits (e.g., Bojitian, Zimudang) possess both Fault and Stratabound Type features (Fig. 1). All Carlin-type gold deposits in the Nanpanjiang Basin have similar host rocks (Triassic organic-rich, dark gray to black silty bioclastic limestone and calcareous siltstone), mineral paragenesis (Pre-ore stage: Fe-rich calcite-detrital quartz, Ore stage: vein quartz, pyrite/arsenopyrite, realgar, and vein calcite), and alteration (decarbonatization, silicification, argillization, sulfidation) (Gu et al., 2013; Su et al., 2018). As noted above, similar to the Carlin-type deposits in Nevada, pyrite is the main host mineral for invisible gold (Su et al., 2018).

Here we focus on the Laizishan and Banqi reservoirs that are spatially associated with the Yata gold deposit (Fig. 3). The pyrobitumen-bearing outcrops are on the southern margin of the Laizishan dome and northern margin of the Banqi dome, ca. 20 km apart. At the Yata deposit, located between the Laizishan and Banqi reservoirs ca. 12 km southwest of the Laizishan dome (Fig. 3), gold-bearing pyrite occurs near the No. 940 mine hole.

3. SAMPLES AND METHODS

Pyrobitumen samples (*n* = 8) were obtained from outcrops of the Laizishan and Banqi reservoirs for Re-Os analysis (Fig. 3) (see Table 1 for detail). The pyrobitumen was sampled from vugs and fracture surfaces in limestone of the Permian Wujiaping Formation. Pyrobitumen occurrences are typically ~2 to 3 cm wide and ~4 to 6 cm long, dark gray to black, associated with calcite, and have smooth and vitreous surfaces (Fig. 4a, c). Samples LZS-3, LZS-6, and LZS-14 come from two different outcrops in the Laizishan reservoir, ca. 6 km west of Ceheng City. Sample LZS-3 and LZS-6 were collected 3 m apart from a ~8-m-long section. About 2 km to the northeast, sample LZS-14 was collected from an open-pit quarry (Fig. 3). Samples BQ-1, BQ-3, BQ-5, BQ-11, and BQ-12 come from the northern margin of the Banqi paleo-reservoir ~4 km north of Banqi village (Fig. 3). Like the samples from the Laizishan reservoir, all of pyrobitumen from the Banqi reservoir is hosted by the Wujiaping Formation limestone. Samples BQ-1, BQ-3, and BQ-5 were collected from the same outcrop with a sampling interval of about 3 m; samples BQ-11 and BQ-12 were taken from an outcrop located ~2 km to the west. All pyrite samples used for Re-Os analysis (n = 9) were collected from a ~10-m-long section at 1 m spacings near the No. 940 mine of the Yata gold deposit, ~2 km east of Yata village (Fig. 3) (see Table 2 for details). Similar to other gold deposits in this area (Lannigou and Banqi deposits), all of the pyrite in the Yata gold deposit is hosted in sandstone and siltstone of the Middle Triassic Xinyuan Formation. The pyrite mainly occurs as disseminated small (10-200 μm) euhedral grains (Fig. 4b, d, g), and locally as massive aggregates (Fig. 4e). Microscopically, pyrite and pyrobitumen exhibit a close textural association with pyrite either surrounding or cross cutting the pyrobitumen (Fig. 4b, d, Fig. S5a) (this study; Wu, 2012) and exhibits a narrow (~ 10 - 20 μm) core-rim texture (Fig. 4h, Fig. S5b) (this study; Wu, 2012).

For the Re-Os analysis, approximately 0.2 to 1.0 g of pyrobitumen was first separated from each sample. All samples were isolated without metal contact, with the pyrobitumen handpicked under a light microscope. The large pyrobitumen grains were crushed to approximately 1 mm using an agate pestle and mortar. For the pyrite samples, the pyrite-bearing sandstone-siltstone samples were first crushed to 200-300 mesh (40-75 μm). After then, more than 0.5 g of the pure pyrite grains (aggregates) with no host rock were handpicked under the light microscope.

The Re and Os isotopic analyses were conducted at the Laboratory for Source Rock and Sulfide Geochemistry and Geochronology, and the Arthur Holmes Laboratory at Durham University following published analytical procedures (Creaser et al., 1991; Völkening et al., 1991; Shirey and Walker, 1995; Selby et al., 2009). Approximately 150 mg of pyrobitumen and ~400 mg pyrite were dissolved and equilibrated with a known amount of mixed ^{185}Re and ^{190}Os spike solution by inverse aqua regia (3 ml HCl + 6 ml HNO_3) in a Carius tube for 24 hr at 220°C. Osmium was isolated and purified from the acidic digestion medium using solvent ($CHCl_3$) and microdistillation methods. The rhenium was isolated from the Os-extracted solution using a NaOH-acetone solvent extraction and HCl–HNO_3-based anion chromatography. Purified Re and Os were loaded onto Ni and Pt filaments, respectively. The Re was measured using Faraday collectors and Os in peak-hopping mode using a secondary electron multiplier, respectively. Measured Re and Os ratios were corrected for oxide contribution and mass fractionation using $^{185}Re/^{187}Re$ = 0.59738 (Gramlich et al., 1973) and $^{192}Os/^{188}Os$ = 3.08261. All data are blank corrected based on the total procedural blank values of Re (1.6 ± 0.5 pg) and Os (150 ± 30 fg), with an average $^{187}Os/^{188}Os$ ratio of approximately 0.22 ± 0.06 (n = 4). All uncertainties include the propagated uncertainty in the standard, spike calibrations, mass spectrometry measurements, and blanks. The mass spectrometer measurements were monitored by solution reference materials (DROsS and Restd). These solutions yielded values of 0.16083 ± 0.00006 for 50 pg aliquot of DROsS and 0.5990 ± 0.0008 (1SD, n = 5) for a 125 pg aliquot of the Re standard, both of which are in good agreement with those previously reported at Durham University (e.g., Saintilan et al. (2018) and references therein). The Re-Os ages were determined using the $^{187}Re/^{188}Os$ and $^{187}Os/^{188}Os$ ratios together with their total 2σ uncertainty and associated error correlation, rho, and with the ^{187}Re decay constant of $1.666x10^{-11}a^{-1}$ (Smoliar et al., 1996), via the program Isoplot v. 4.15 (Ludwig, 2008).

In order to determine the gold content of the pyrite samples, eight polished sections were selected for Electron probe microanalysis (EPMA) (Table 3). They were analyzed using a JEOL JXA-8230 electron microprobe at the Laboratory of Microbeam Analysis Technology Limited Company, Wuhan. Prior to analysis, the samples were firstly coated with ca. 20 nm thick conductive carbon film following published analytical procedures (Zhang and Yang, 2016). The abundance of gold (Au), As, Fe, S, Ag, Sb, Zn and Cu in pyrite was determined using an accelerating voltage of 20 kV, analysis diameter of 1 μm and probe current of 20 nA. The peak counting time was 10 s for Cu, S, Fe, Sb, Ag, As, Zn and 120 s for Au. The background counting time was half of the peak counting time. The standards used are Copper (Cu), Pyrite (S, Fe), Antimony (Sb), Silver (Ag), Gold (Au), Gallium Arsenide (As), and Zinc (Zn).

4. RESULTS

4.1 Rhenium–Osmium data for Laizishan and Banqi reservoir pyrobitumen

The Re and Os abundance of the pyrobitumen samples range from 5 to 283 ppb and 209 to 2360 ppt, respectively (Table 1). These values are significantly higher than those of average upper crustal values (Re = 0.2-1 ppb, Os = 31 ppt (Esser and Turekian, 1993; Peucker‐Ehrenbrink and Jahn, 2001)), but similar to previously reported values for pyrobitumen (Ge et al., 2016). The $^{187}Re/^{188}Os$ values of the pyrobitumen range between 67.6 and 683.0 and exhibit a radiogenic $^{187}Os/^{188}Os$ composition of 0.82 to 3.21 (Table 1). The Re-Os isotopic data of the eight pyrobitumen samples yield a Model 3 Re-Os age of 236 ± 36 Ma, with an initial $^{187}Os/^{188}Os$ composition [Os_i] of 0.42 ± 0.28 (Fig. 5). This Model 3 result assumes that the scatter about the best-fit line is a combination of the assigned uncertainties and an unknown, but normally distributed, variation in the $^{187}Os/^{188}Os$ values (Ludwig, 2008).

4.2 Rhenium–osmium data for Yata gold deposit pyrite

The Re and Os (^{192}Os) abundances for the pyrite samples are 0.6 to 7.9 ppb and 29 to 106 (11–33) ppt, respectively (Table 2). These abundances are similar to pyrite reported in other metal deposits (Lawley et al., 2013; Zimmerman et al., 2014; Hnatyshin et al., 2015; Kelley et al., 2017). The $^{187}Re/^{188}Os$ and $^{187}Os/^{188}Os$ values of the pyrite range from 115.5 to 556.6 and from 1.0 to 2.8, respectively (Table 2). The Re-Os data of the nine samples yield a Model 3 age of 233 ± 42 Ma, with Os_i of 0.59 ± 0.26 (Fig. 6).

4.3 Electron probe microanalysis data for Yata gold deposit pyrite

The EPMA data of the pyrite samples which were selected for Re-Os analysis are presented in Table 3. In these samples the abundance of Au, As, Ag, Sb, Zn, and Cu is variable and exhibit the following general trend As > Au > Cu > Zn > Ag > Sb (Table 3). The As and Au abundance ranges from 300 to 58,400 ppm (average = 9400 ppm) and 90 to 800 ppm (average = 345 ppm), respectively. For the remaining elements (Ag, Sb, Zn, Cu) the abundances are very low with some analyses below detection limit (Ag up to 300 ppm, average = 130 ppm; Sb = 100 to 200 ppm, average = 118 ppm; Zn = 100 to 300 ppm, average = 150 ppm; Cu = 100 to 300 ppm, average = 165 ppm). In agreement to previous studies, the dominant location of the gold is within fine-grained pyrite and narrow pyrite rims (Fig. 4g, h). Although Au could be detected in some pyrite cores, there is a clear decreasing trend of Au abundance from the rim to the core (Fig. 4h).

5. DISCUSSION

5.1 Timing of dry gas generation in Nanpanjiang Basin

Hydrocarbon generation is a step-by-step process involving the production of liquid oil initially, which with increased temperature thermally cracks to form gas and pyrobitumen (Lewan, 1985). In the Nanpanjiang Basin (i.e., the Banjie, Anran, Balai, Laizishan reservoirs), the solid bitumen exhibits the following characteristics, insoluble in organic solvents (Zhao et al., 2007), low H/C ratio (0.17-0.52) (Zhao et al., 2007), high bitumen reflectance (BRo, %) (2.85-6.25 %) (Zhuang et al., 2000; Zhao et al., 2007), mosaic structure and straight and clear boundary of the bitumen under microscope (Zhao et al., 2007) and organic geochemistry ratios of $C_{29}\alpha\alpha\alpha$ 20S/(20S+20R) of 0.62-0.78, $C_{29}\beta\beta/(\beta\beta+\alpha\alpha)$ of 0.31-0.48, and a methylphenanthrene index (MPI-1) of 0.38-1.00 (equal to a Ro of 1.7-2.1%) (Table S5)(Wu, 2012). These features indicate that the solid bitumen is high hydrocarbon maturity pyrobitumen that formed from the cracking of liquid oil (Seifert and Moldowan, 1986; Chen and Jin, 1995; Peters et al., 2005; Zhao et al., 2007; Wu, 2012). Any gas reservoirs formed as a result of the thermal cracking of oil in the Nanpanjiang Basin are considered to have been lost through uplift and erosion. However, methane is present and comprises more than 80 % of the gas phase in gas-bearing fluid inclusions in existing reservoirs (Gu et al., 2012), and occur with coeval aqueous fluid inclusions that yield an average homogenization temperature (T_h) > 150°C (Zhao et al., 2006a; Gu et al., 2012).

All of the pyrobitumen Re-Os data from the Laizishan and Banqi reservoirs collectively yield a Re-Os age of 236 ± 36 Ma (n = 8, initial $^{187}Os/^{188}Os$ ratio [Os_i] = 0.42 ± 0.28, Mean Squared Weighted Deviates [MSWD] = 871) (Fig. 5). The large age uncertainty and MSWD value suggest that the sample set does not fully meet the criteria for developing a robust isochron, which requires that (1) all samples formed contemporaneously, (2) all samples possess the same Os_i value, and (3) the isotope systematics have not been disturbed (Cohen et al., 1999; Kendall et al., 2009). Calculated Os_i values using the Re-Os age of 236 Ma show that samples LZS-3, BQ-5, and LZS-6 have less-radiogenic values (0.17, 0.32, and 0.36, respectively), compared to the remaining samples that possess more similar and radiogenic Os_i values (0.49-0.56; avg Os_i = 0.52 ± 0.03), with the exception of BQ-11 (0.43; including BQ-11 avg Os_i = 0.50 ± 0.05) (Table.1). As such, the scatter about the best-fit line of the Re-Os data is a function of the data set having variable Os_i values (e.g., samples LZS-3, BQ-5, LZS-6). Although hard to confirm, the relatively long intervals of both initial oil generation from the source rock and the later pyrobitumen and gas generation during oil cracking, could result in the samples not being formed contemporaneously, and as a result could cause variations in Os_i, as well as the large age uncertainty and MSWD values (Lillis and Selby, 2013; Ge et al., 2016). The Re-Os data for samples BQ-1, 3, 11, 12, and LZS-14 yield a Re-Os age of 228 ± 16 Ma (n = 5, Os_i = 0.56 ± 0.13, MSWD = 47) (Fig. 5). Although an isochron age determined from two samples is not a robust reflection of the true geologic age (Ludwig, 2008), the Re-Os data for samples BQ-5 and LZS-6 yield a Re-Os age of 229.7 ± 4.0 Ma (Os_i = 0.39 ± 0.03) (Fig. 5), which is similar to that determined for samples BQ-1, BQ-3, BQ-11, BQ-12, and LZS-14.

Basin modelling of strata in the Yang 1 well, ~15 km southeast of our study area (Fig. 1), suggests that the Devonian source rocks entered the oil window (~2 km depth, Ro: 0.6-1.0 %) during the Late Carboniferous, with peak oil generation occurring in the Permian (Zhao et al., 2006b). However, rapid subsidence driven by the Indochina-South China collision from the Late Permian to Early Triassic resulted in the Permian limestone being buried to >5 km (Zhao et al., 2006b; Zaw et al., 2014) (Fig. 7). Burial modelling and hydrocarbon maturation analysis of the Devonian shale in the Nanpanjiang Basin indicate that the shale began to generate dry gas during the Middle Triassic (Zhou, 1999). According to the temperature gradient in South China (Hu et al., 2000), temperatures of the Late Permian reservoir could have reached more than 200°C, which is consistent with the homogenization temperatures (> 150 °C) for aqueous fluid inclusions coeval with methane-dominated fluid inclusions (Zhao et al., 2006a; Gu et al., 2012). Such temperatures would have resulted in the thermal cracking of any liquid oil. In summary, basin modelling indicates that oil generation and accumulation happened before the Middle Triassic, with thermal cracking of the reservoir oil occurring following rapid subsidence of the Nanpanjiang Basin after the mid-Triassic (Zhao et al., 2006b).

Studies have found that the Re-Os systematics of highly mature hydrocarbons in the Bighorn Basin, USA (Lillis and Selby, 2013), and bitumen in the North Hebei depression, China (Li et al., 2017), may exhibit disturbance. Moreover, Re-Os dating of pyrobitumen that formed contemporaneously with methane in the Majiang-Wanshan reservoir, Xuefeng uplift, the Micang Shan reservoir, northern Sichuan Basin as well as the Ziyang-Weiyuan-Anyue gas field, central Sichuan Basin in the South China block, show that the pyrobitumen Re-Os age coincides with the timing of gas generation (Ge et al., 2016; Ge et al., 2018; Shi et al., 2020). The Re-Os age of 228 ± 16 Ma determined here for pyrobitumen from the Laizishan and Banqi reservoirs is younger than that inferred for liquid oil generation (Zhao et al., 2006b), but is within uncertainty and in agreement with the estimated timing of the thermal cracking of liquid oil, thus further suggesting that pyrobitumen Re-Os ages yield the timing of gas, not oil, generation.

5.2 Timing of gold mineralization in the Nanpanjiang Basin

Establishing the mineralogical residence of the gold and its distribution within Carlin-type deposits has been an on-going challenge since the discovery of the deposit type in the 1960s (Zhang, 1997; Bidari and Aghazadeh, 2018; Cline, 2018). Gold could be contained within chalcopyrite and sphalerite (Wells and Mullens, 1973), cinnabar, illite and quartz (Bakken et al., 1989; Cline et al., 2005) in this deposit type. However, because of both scarcity and low gold contents of these minerals, they are not considered to be the major gold host. It is now generally accepted that invisible gold in Carlin-type deposits is encapsulated in sulfides and clays (Hausen, 2000) and that pyrite is the most common gold-bearing sulfide (Au abundance could exceed 1000 ppm) (Cline et al., 2005; Cline, 2018; Su et al., 2018; Xie et al., 2018a). Although the majority of gold in Carlin-type systems in both Nevada and the Nanpanjiang Basin is ionically bound in the pyrite lattice either as micrometer-scale (<10 μm) grains or within rims of otherwise gold-poor pyrite (Fig. 4g, h) (Su et al., 2012; Cline, 2018), in the Nanpanjiang Basin gold-bearing pyrite is texturally and chemically distinct from that of gold-bearing pyrite in Nevada. For example, ore pyrite in Carlin-type systems of Nevada occurs as rims or interstitial grains and can be readily observed under the microscope. In contrast, in the Nanpanjiang Basin, auriferous pyrite rims are indistinguishable microscopically from the pyrite core because of similar color, relief, and reflectivity. Yet, textural characteristics are however better distinguished by BSE imagery (Fig. 4h), EPMA, and laser ablation-ICP-MS analyses (Xie et al., 2018a). In addition to gold, the rim of pyrite in the Carlin-type systems of Nevada are enriched in As, Hg, Tl, Cu, and Sb, relative to the core (Xie et al., 2018a). Although all of these elements are detected in ore pyrite of the Nanpanjiang Basin, the concentrations are much lower (Table 3) (Xie et al., 2018a). In summary, the morphology and chemical differences of gold-bearing pyrite from Carlin-type deposits in Nevada and those in the Nanpanjiang Basin suggest that the two systems formed from fluids having different characteristics (Xie et al., 2018a). In the Nanpanjiang Basin, subtle variations both in morphology and geochemistry features in the pyrite core and rim indicate they were formed during one continuously evolving hydrothermal event (Xie et al., 2018a) and thus dating the gold-bearing pyrite could help constrain the timing related to this hydrothermal event and the formation of the gold deposits.

All of the Re-Os data for the pyrite from the Yata gold deposit yield an age of 233 ± 42 Ma (n = 9, Os_i = 0.59 ± 0.26, MSWD = 59) (Fig. 6). Importantly, the large age uncertainty and MSWD value are controlled by two samples (YT-42 and YT-46) that deviate from the best-fit line (Fig. 6). The calculated Os_i using the Re-Os age of 233 Ma yields values of 0.35 and 0.81 for samples YT-46 and YT-42, respectively (Table 2). The Re-Os data for the remaining seven samples produces a more precise Re-Os age of 218 ± 25 Ma (n = 7, Os_i = 0.67 ± 0.16) and lower MSWD (8.1) (Fig. 6). However, the Os_i values calculated at 218 Ma for samples YT-46 (0.42) and YT-42 (0.93) are still significantly different (Table 2). The later maybe explained by impurities in mineral separates, open-system behavior of the Re-Os isotopic system (Nakai et al., 1993), mixing of different generations of sulfide and / or prolonged mineralization (Hnatyshin et al., 2015; Hnatyshin et al., 2020). Given that the sampled pyrite grains, for example YT43 and YT42, are mixture of core and rim pyrite (micro-meter scale that are impossible to separate (Fig. 4h)) that formed as a result of a continuously evolving hydrothermal event (Xie et al., 2018a), a prolonged mineralization duration and / or mixing of different generations of pyrite, may cause the differences observed in the Os_i compositions of pyrite from the Yata deposit, which ultimately results in the large age uncertainty.

The pyrite samples from the Yata deposit were collected from siltstone of the Xinyuan Formation of the Middle Triassic Anisian stage. Although the pyrite Re-Os age of 218 ± 25 Ma has a relatively large uncertainty, the nominal Re-Os age is in good agreement with (1) a Rb-Sr age of 212.8 ± 4.6 Ma determined on hydrothermal, gold-bearing, fine-grained (3-5 μm) illite from the Yata deposit (Table S1, Fig. S1a) (Jin, 2017); (2) an *in situ* SIMS U-Pb age of 213.6 ± 5.4 Ma for hydrothermal rutile from the Zhesang gold deposit, ~100 km south of Yata (Fig. 1) (Pi et al., 2017); and (3) Re-Os arsenopyrite ages of 204 ± 19 Ma, 206 ± 22 Ma and 235 ± 33 Ma for the Lannigou, Jinya, and Shuiyindong deposits in the Nanpanjiang Basin (Chen et al., 2015). Collectively, the Re-Os, Rb-Sr, and U-Pb Late Triassic ages may indicate the beginning of Carlin-type gold mineralization in the Nanpanjiang Basin. Whereas older isotope ages, for example Rb-Sr ages (235 ± 9.3 Ma)on coarse-grained (5-10 μm) illite for the Yata deposit (Table S1, Fig. S1b) (Jin, 2017), Rb-Sr ages on fluid inclusions in the Jinya deposit (276 ± 28 Ma; Wang, 1992) and the Lannigou deposit (259 ± 27 Ma; Hu et al., 1995), which are in some cases older than the host sedimentary strata (Middle Triassic), do not record the time of mineralization. Younger ages (<200 Ma), for example an Ar-Ar sericite age for the Lannigou deposit (194.6 ± 2 Ma; Chen et al., 2009), Rb-Sr age for realgar-bearing quartz from the Yata deposit (148.5 ± 4.1 Ma)(Table.S2, Fig. S2) (Jin, 2017), and Sm-Nd ages on calcite and fluorite from the Shuiyindong, Nibao, and Shitouzhai deposits (122-180 Ma) (Table S3, S4; Fig. S3, S4)(Su et al., 2009; Gu et al., 2012; Jin, 2017), likely record hydrothermal activity that post-dates the main episode of gold mineralization or its termination (Fig. 8) (Su et al., 2009; Gu et al., 2012; Jin, 2017). The latter interpretation is further supported by petrography, EPMA, and XRD analysis that show that the hydrothermal sericite in the

Yata deposit is bereft of gold and post-dates gold deposition (Chen et al., 2009). As such, the Early Jurassic (ca. 195 Ma) Ar-Ar sericite age for the Lannigou deposit could represent the waning stages of hydrothermal activity of the Carlin-type gold systems in the region.

5.3 Relationship between hydrocarbons and gold mineralization

It is well documented that metals are associated with crude oil and solid bitumen in many sedimentary basins (Kesler et al., 1994; Wilson and Zentilli, 2006; Emsbo and Koenig, 2007; Gu et al., 2010). The oil and bitumen in the MVT Pb-Zn deposits are considered to be the source for the reduced sulfur required to precipitate the sulfide ores through either direct release of organically bound sulfur in Cincinnati arch, USA (Kesler et al., 1994) or thermochemical reduction of sulfate from basinal fluids or evaporates in Pine Point, Canada (Powell and Macqueen, 1984). Paragenetic and geochemical analysis of the manto-type copper deposits, central Chile suggest pyrobitumen may act as a reductant for the mineralizing fluids (Wilson and Zentilli, 2006). The Laser ablation ICP-MS analyses on the bitumen in the El Rodeo deposit, USA, which showed that bitumen could contain up to 100 ppm Au, were used to suggest Au and associated metals could be remobilized and transported as organo-metallic compounds during oil generation and migration (Emsbo and Koenig, 2007). In addition, more recent empirical evidence suggests that petroleum may have acted as an important fluid during ore formation (Migdisov et al., 2017) and this has been an overlooked frontier in ore genesis research (Williams-Jones et al., 2009). In a water-oil-rock system, gold has been experimentally shown to predominantly enter the oil phase (Zhuang et al., 1998). Furthermore, recent experiments show metal (Zn, Au, U) abundance in crude oils increases from 100 to 200 - 250°C, peaking at ca. 200 - 250 °C (50 ppb for Au), and then begins to decrease at > 250°C - 300 °C (Migdisov et al., 2017). Although largely qualitative, this result provides insight into the behavior of metals in liquid hydrocarbons and indicates that liquid hydrocarbons have the potential to mobilize and concentrate metals. Specifically the experimental conditions show that as a liquid oil begins to convert to pyrobitumen and natural gas at elevated temperatures (> 160 °C) (Williams-Jones et al., 2009; Zhu et al., 2013), the decrease in metal abundance in the hydrocarbon (Migdisov et al., 2017) coincides with the conditions of thermal cracking of oil. In summary, the experiment indicates that metals (Zn, Au, U) can be enriched in liquid oil, but these metals will be released to the fluid phase during the thermal cracking of oil (Zhuang et al., 1998; Emsbo and Koenig, 2007; Migdisov et al., 2017; Crede et al., 2019).

Homogenization temperatures (T_h) of fluid inclusions in diagenetic calcite from the Permian hydrocarbon reservoirs in the Nanpanjiang Basin range from ~70°C to 220°C (Zhao et al., 2006a; Gu et al., 2012). Specifically, early stage aqueous fluids inclusions that are coeval with the oil-bearing fluid inclusions are characterized by low T_h (73-87°C, mean 80°C). In contrast, late stage aqueous fluid inclusions that are coeval with the methane-dominated inclusions possess high T_h (110-180°C, mean > 150°C), and reflect the thermal cracking of liquid oil (Gu et al., 2012) (Fig. 9).

Fluid inclusion analysis from different mineralization stages of the Carlin-type gold deposits in the Nanpanjiang Basin show a decreasing trend in T_h data from ca. 230°C during the gold-bearing pyrite stage to ca. 150°C during the post-gold, vein realgar-calcite stage (Hu et al., 2002; Gu et al., 2012; Su et al., 2018). The temperatures of thermal cracking of oil and main gold mineralization that occurred in the Nanpanjiang Basin could be a continuous process with oil cracking being post-dated by pyrite formation during the increase in temperature. In addition, similar mass chromatogram characteristics of sterane and terpane (for example GAM/H_{30} ratio (0.14 vs 0.14), H_{32} S/(R+S) ratio (0.51 vs 0.52) and similar V shape distribution of C_{27}, C_{28}, C_{29} steranes with C_{29} sterane exhibiting the highest abundance) for pyrobitumen either from the paleo-reservoirs or gold deposits from Nanpanjiang Basin indicate they are from same source (Table S5) (Wu, 2012). Both pyrobitumen and pyrite occur in the pore spaces of the limestone in the Laizishan reservoir (Fig. 4b, d) with pyrite observed to cross cut pyrobitumen in the Shuiyindong gold deposits, Nanpanjiang Basin (Fig, S5a) (Wu, 2012). All the above features indicate that pyrobitumen formation by thermal cracking as well as gold mineralization is broadly coeval, including the possibility that the pyrobitumen formed slightly earlier than the gold-bearing pyrite. Our Re-Os dating supports this temporal relationship between pyrobitumen formation (228 ± 16 Ma) and gold mineralization (218 ± 25 Ma), in which the pyrobitumen is nominally older, but with both events occurring during peak burial temperatures (>200°C) within strata of the Nanpanjiang Basin. The proposed origin of the gold involving the thermal cracking of liquid oil is potentially also supported by the similar Os_i values of the pyrobitumen (0.58-0.72) and pyrite (0.59-0.76). In our model, during burial of the Permian reservoir to more than 5 km (>150 °C condition) the oil thermally cracked, with the spatially associated fluids incorporating not only the gold, but also the osmium isotope composition from the thermally cracked oil.

Given that gold in Carlin-type gold deposits worldwide mainly resides in pyrite (Cline, 2018; Muntean, 2018a; Su et al., 2018), the mechanism that leads to precipitation of the gold-bearing pyrite is important to consider. Petrographic and geochemical evidence from the northern Carlin trend indicate sulfidation between Fe-dolomite and Au and H_2S rich ore fluid was the most important mechanism of gold deposition in Carlin-type deposits (Emsbo et al., 2003). As mentioned above, the major host rock at the Lannigou and Yata gold deposits is Fe-rich calcareous and dolomitic siltstone. Scanning electron microscopy-energy dispersive spectroscopy (SEM-EDS) of samples from the Lannigou deposit indicate that iron concentrations in the Fe dolomite range between 11 and 17 wt % (Xie et al., 2018a), which via leaching by hydrothermal fluids could have provided sufficient iron for pyrite formation. Lithogeochemical studies of the Shuiyindong gold deposits suggests that the gold and associated trace elements were also transported in H_2S-rich fluids (Su et al., 2009; Su et al., 2018). Together with the observed replacement of ferroan calcite and dolomite in the host rocks by arsenian pyrite and illite, gold-bearing ore pyrite is also attributed to have formed from a H_2S-rich ore fluid via sulfidation of local Fe-bearing minerals in the Nanpanjiang Basin (Su et al., 2018).

Although a magmatic source of sulfur for the gold deposits is considered (Xie et al., 2018b), the lack of coeval intrusions and only being distal to the gold deposits may indicate the possibility of a sedimentary derived sulfur component In the Nanpanjiang Basin (Hu et al., 2002). As to the formation of the H_2S, the broad range of S isotope values in the Carlin type gold deposits lead to proposal of several mechanisms, such as the dissolution of diagenetic pyrite, desulfidation of pyrite to pyrrhotite, thermochemical sulfate reduction and the destruction of organosulfur compounds (Emsbo et al., 2003; Cline et al., 2005; Large et al., 2011). The $\delta^{34}S$ values of ore pyrite from gold deposits in our study area are also variable (Su et al., 2018). Previous studies show ore pyrite $\delta^{34}S$ values of 7.3 - 12.6‰, -2.3 - 8.0‰, and ca. 9.0‰ in the Laizishan, Yata and Banqi gold deposits, respectively (Zhang, 1997; Su et al., 2018). Although some sulfur isotope data overlap with the range of magmatic sulfur (-2.5 - 5.1‰) (Seal, 2006), the overall variability of the sulfur isotope values suggests that H_2S in the ore fluids was probably derived from sedimentary rocks. Therefore, the thermochemical sulfate reduction (TSR), with the reaction between organic matter (oil and gas) and sulfate at elevated temperatures (>140^{o}C) with the formation of carbonate (CO_3^{2-}), carbon dioxide (CO_2) and H_2S, could be a significant process (Machel, 2001; Cai et al., 2004; Hao et al., 2015). Because the bond energy of ^{32}S-O is lower than that of ^{34}S-O, more $^{32}SO_4^{2-}$ relative to $^{34}SO_4^{2-}$ will take part in the TSR process, leading to the sulfide having a relatively lighter sulfur isotope composition compared with coeval sulfate (Zhu et al., 2005). Previous work has found that the sulfur isotope difference between sulfide and sulfate ($\Delta^{34}S$) decreases from ~20 to 10 ‰ as temperature increases from 100 ^{o}C to >200 ^{o}C (Machel et al., 1995). Sulfur isotope data for the ore-stage pyrite ($\delta^{34}S$ ~20 ‰) in the Post/Betze gold deposit and Paleozoic seawater sulfates represented by stratiform barite (20-35‰) in Nevada, indicate that TSR may be an important mechanism for the source of sulfur (Arehart et al., 1993; Emsbo and Hofstra, 2003). Similar to the Carlin-type gold deposits in Nevada, a stratiform barite deposit (e.g., Zhenning deposit, ~100 km north of Yata gold deposit) is present in Devonian strata within the Nanpanjiang Basin, which exhibits a mean $\delta^{34}S$ value of ca. 37‰ (Hu et al., 2002; Gao et al., 2017). The sulfur isotope values of the hydrothermal pyrite in the Lannigou and Yata gold deposits (4.7 to 12.0 ‰, (Zhang et al., 2003; Su et al., 2018)) are lighter than those of seawater sulfate in the Triassic (ca. 10-15‰) (Claypool et al., 1980) and that of barite from the Zhenning deposit. In addition to Carlin-type gold deposits, the pyrite sulfur isotope values for other sediment-hosted gold deposits worldwide show a similar pattern with the contemporaneous seawater sulfate curve, in which $\delta^{34}S$ values are ca. 15 to 20 ‰ lower than that of coeval seawater sulfate, considered by most workers to reflect the reduction of seawater sulfate (Chang et al., 2008). In summary, the lighter $\delta^{34}S$ value of the pyrite in the gold deposits, compared with that of coeval seawater sulfate or the barite, may record TSR processes during the gold-bearing pyrite formation in the Nanpanjiang Basin. Sulfur and carbon isotope analysis of the hydrogen sulfide, carbonate, and calcite in the H_2S-rich natural gas field in the South China block indicate that the H_2S could be derived via TSR between the thermally cracked gas and sulfate (Cai et al., 2004; Zhu et al., 2005; Hao et al., 2015). Moreover, a positive shift in the $\delta^{13}C$ value of methane, which is isotopically heavier than the CO_2, suggests that the methane is the major reactant for the TSR process in a high C_1/C_{1-6} ratio (>0.95) environment (Worden and Smalley, 1996; Pan et al., 2006; Cai et al., 2013). In the Nanpanjiang Basin, the much higher basin burial temperature (>200^{o} C) led to the thermal cracking of liquid oil into pyrobitumen and methane. Laser Raman spectroscopic analyses of fluid inclusions from calcite in strata of the Laizishan reservoir find CH_4 to be the predominant gas (Gu et al., 2007b). The negative relationship between CO_2 and CH_4 volume in fluid inclusions of the Laizishan reservoir (Gu et al., 2007a) also supports the premise that CH_4 could be involved in the TSR process (Fig. 9). Collectively, the above data support CH_4-dominated TSR in the Nanpanjiang Basin, as also inferred for the Carlin-type gold deposits in the study area.

Integrating all the above data, the relationship between the different types of hydrocarbons (oil and gas) and the formation of the Carlin type gold deposits in the Nanpanjiang Basin is summarized below (Fig. 9). From the Late Carboniferous to Early Triassic, the Devonian source rocks underwent burial and entered the oil window (~120 ^{o}C). During the hydrocarbon (oil) expulsion and migration process from the source to the reservoir, the liquid oil absorbed metals (including Au) sourced from either sedimentary rocks (Hofstra and Cline, 2000) or igneous activity (Zhu et al., 2020)(Fig. 9a). Rapid subsidence driven by the Indochina-South China collision from the Late Permian to Early Triassic resulted in burial of the Permian reservoir to >5 km with temperatures reaching more than 200°C, which led to the thermally cracking of liquid oil and the generation of the pyrobitumen and gas (methane dominated) during the Late Triassic (Fig. 9b). Then, a methane dominated TSR process began and resulted in an increase of reduced sulfur (H_2S) in the fluid. At the same time, the gold released during the cracking of the oil formed a bisulfide complex ($Au(HS)^0/Au(HS)_2^-$) with the sulfur in the fluid (Fig. 9b). Finally, when the Au and H_2S rich ore fluid reached the Triassic Fe-rich calcareous and dolomitic siltstone in the Nanpanjiang Basin, sulfidation between bisulfide and iron finally caused the formation of the disseminated gold-bearing pyrite (gold deposit) (Fig. 9c).

6. CONCLUSIONS

Integrating Re-Os isotope pyrobitumen and gold-bearing pyrite data, this study quantitatively constrains the evolution of hydrocarbon (oil and gas) and gold mineralization in the Nanpanjiang Basin. The Re-Os age for the highly mature pyrobitumen from the Laizishan and Banqi reservoirs (228 ± 16 Ma) coincides with results of basin modelling for the Nanpanjiang Basin, suggesting that the pyrobitumen and dry gas formed during the early Late Triassic through the thermal cracking of liquid oil. The broadly identical Re-Os age for gold-bearing pyrite from the Yata deposit (218 ± 25 Ma), which is in agreement with *in situ* SIMS U-Pb rutile (213.6 ± 5.4 Ma), Re-Os arsenopyrite (204 ± 19 Ma - 235 ± 33 Ma), and Rb-Sr illite (212.8 ± 4.6 Ma) ages for other Carlin-type gold deposits in the Nanpanjiang Basin, further supports a model for gold mineralization during the Late Triassic.

The contemporaneity of the Re-Os pyrobitumen and gold-bearing pyrite ages (228 ± 16 and 218 ± 25 Ma) obtained in this study, coupled with recent experimental data highlighting the uptake and release of metals from hydrocarbons and fluid inclusion data for both hydrocarbon reservoir and gold deposits in the Nanpanjiang Basin, suggest that methane-dominated TSR may be one key formational mechanism for the Carlin-type gold deposits in this basin (Fig. 9). In our model, the produced methane from the thermal cracking of oil reacted with sulfate, resulting in an increase in reduced sulfur (H_2S) in the fluid. At the same time, the gold released from the oil complexed with the sulfur ($Au(HS)^0$/ $Au(HS)_2^-$) in ore bearing fluid. Finally, when the Au and H_2S rich ore fluid reached the Triassic Fe-rich strata in the Nanpanjiang Basin, sulfidation between bisulfide and iron caused the formation of the gold-bearing pyrite mineralization.

ACKNOWLEDGMENTS

This work was supported by the National Natural Science Foundation of China (No.41802168, 41672140, 41372140), the PetroChina Innovation Foundation (No.2016D-5007-0103), the Program of Introducing Talents of Discipline to Universities (No.B14031), the Outstanding Youth Funding of Natural Science Foundation of Hubei Province (No. 2016CFA055), and the Fundamental Research Fund for the Central Universities, China University of Geosciences (Wuhan, No. CUG180617, CUGCJ1820, CUGCJ1712), and Open Topic Fund from Key Laboratory of Tectonics and Petroleum Resources of Ministry of Education (TPR-2018-11). Science and technology project of Guizhou province (No. [2018]1065). DS acknowledges the Total Endowment Fund and the Dida Scholarship from CUG Wuhan. We also thank

John Slack, Balz Kamber, David van Acken and one anonymous reviewer for providing insightful comments and suggestions that improved this manuscript.

REFERENCES

Anderson, G.M., 1975. Precipitation of Mississippi Valley-type ores. Economic Geology, 70: 937-942.

Arehart, G.B., Eldridge, C.S., Chryssoulis, S.L., Kesler, S.E., 1993. Ion microprobe determination of sulfur isotope variations in iron sulfides from the Post/Betze sediment-hosted disseminated gold deposit, Nevada, USA. Geochimica et Cosmochimica Acta, 57(7): 1505-1519.

Bakken, B.M., Hochella, M.F., Marshall, A., Turner, A., 1989. High-resolution microscopy of gold in unoxidized ore from the Carlin mine, Nevada. Economic Geology, 84(1): 171-179.

Bidari, E., Aghazadeh, V., 2018. Pyrite from Zarshuran Carlin-type gold deposit: Characterization, alkaline oxidation pretreatment, and cyanidation. Hydrometallurgy, 179: 222-231.

Cai, C. et al., 2004. Methane-dominated thermochemical sulphate reduction in the Triassic Feixianguan Formation East Sichuan Basin, China: Towards prediction of fatal H_2S concentrations. Marine and Petroleum Geology, 21(10): 1265-1279.

Cai, C., Zhang, C., He, H., Tang, Y., 2013. Carbon isotope fractionation during methane-dominated TSR in East Sichuan Basin gasfields, China: A review. Marine and Petroleum Geology, 48: 100-110.

Cai, J.-X., Zhang, K.-J., 2009. A new model for the Indochina and South China collision during the Late Permian to the Middle Triassic. Tectonophysics, 467(1): 35-43.

Chang, Z., Large, R.R., Maslennikov, V., 2008. Sulfur isotopes in sediment-hosted orogenic gold deposits: Evidence for an early timing and a seawater sulfur source. Geology, 36(12): 971-974.

Chen, M., Huang, Q., Hu, Y., Chen, Z., Zhang, W., 2009. Genetic types of phyllosilicate (micas) and its ^{39}Ar-^{40}Ar dating in Lannigou gold deposit, Guizhou Province, China. Acta Mineralogica Sinica, 29(3): 353-362.

Chen, M., Mao, J., Li, C., Zhang, Z., Dang, Y., 2015. Re–Os isochron ages for arsenopyrite from Carlin-like gold deposits in the Yunnan–Guizhou–Guangxi “golden triangle”, southwestern China. Ore Geology Reviews, 64(1): 316-327.

Chen, Z., Jin, K., 1995. Organic petrology characteristics of nature sollid bitumens. Coal Geology & exploration, 23(4): 18-22.

Claypool, G.E., Holser, W.T., Kaplan, I.R., Sakai, H., Zak, I., 1980. The age curves of sulfur and oxygen isotopes in marine sulfate and their mutual interpretation. Chemical Geology, 28: 199-260.

Cline, J.S., 2018. Nevada’s Carlin-type gold deposits: What we’ve learned during the past 10 to 15 years. In: Muntean, J.L. (Ed.), Diversity in Carlin-style gold deposits. Society of Economic Geologists Special Publications, v.20, pp. 7-37.

Cline, J.S., Hofstra, A.H., Muntean, J.L., Tosdal, R.M., Hickey, K.A., 2005. Carlin-type gold deposits in Nevada: Critical geologic characteristics and viable models. Economic Geology, 100th anniversary volume: 451-484.

Cohen, A.S., Coe, A.L., Bartlett, J.M., Hawkesworth, C.J., 1999. Precise Re–Os ages of organic-rich mudrocks and the Os isotope composition of Jurassic seawater. Earth and Planetary Science Letters, 167(3): 159-173.

Creaser, R., Papanastassiou, D., Wasserburg, G., 1991. Negative thermal ion mass spectrometry of osmium, rhenium and iridium. Geochimica et Cosmochimica Acta, 55(1): 397-401.

Crede, L.-S. et al., 2019. Crude oils as ore fluids: An experimental in-situ XAS study of gold partitioning between brine and organic fluid from 25 to 250°C. Geochimica et Cosmochimica Acta, 244: 352-365.

Du, Y. et al., 2013. The basin translation from Late Paleozoic to Triassic of the Youjiang Basin and its tectonic signification. Geological Review, 59(1): 1-11.

Emsbo, P., Hofstra, A.H., 2003. Origin and significance of postore dissolution collapse breccias cemented with calcite and barite at the Meikle gold deposit, northern Carlin trend, Nevada. Economic Geology, 98(6): 1243-1252.

Emsbo, P., Hofstra, A.H., Lauha, E.A., Griffin, G.L., Hutchinson, R.W., 2003. Origin of high-grade gold ore, source of ore fluid components, and genesis of the Meikle and neighboring Carlin-type deposits, northern Carlin trend, Nevada. Economic Geology, 98(6): 1069-1105.

Emsbo, P., Koenig, A.E., 2007. Transport of Au in petroleum: Evidence from the northern Carlin trend, Nevada, Dublin. Millpres, Proceedings of the 9th Biennial SGA Meeting, Dublin, pp. 695.

Esser, B.K., Turekian, K.K., 1993. The osmium isotopic composition of the continental crust. Geochimica et Cosmochimica Acta, 57(13): 3093-3104.

Fetter, N. et al., 2019. Lead isotopes as tracers of crude oil migration within deep crustal fluid systems. Earth and Planetary Science Letters, 525: 115747.

Fuchs, S., Williams-Jones, A.E., Jackson, S.E., Przybylowicz, W.J., 2016. Metal distribution in pyrobitumen of the Carbon Leader Reef, Witwatersrand Supergroup, South Africa: Evidence for liquid hydrocarbon ore fluids. Chemical Geology, 426: 45-59.

Gao, J. et al., 2017. Forming mechanism analysis of the abnormally high $\delta^{34}S$ baryte deposits: A case study from the Zhenning–Ziyun large Devonian baryte deposits, Guizhou Province, China. Geomicrobiology Journal, 34(6): 481-488.

Ge, X., Shen, C., Selby, D., Deng, D., Mei, L., 2016. Apatite fission-track and Re-Os geochronology of the Xuefeng uplift, China: Temporal implications for dry gas associated hydrocarbon systems. Geology, 44(6): 491-494.

Ge, X. et al., 2018. Neoproterozoic-Cambrian petroleum system evolution of the Micang Shan uplift, northern Sichuan Basin, China : Insights from pyrobitumen Re-Os geochronology and apatite fission track analysis. AAPG Bulletin, 102(8): 1429-1453.

Georgiev, S.V. et al., 2016. Re–Os dating of maltenes and asphaltenes within single samples of crude oil. Geochimica et Cosmochimica Acta, 179: 53-75.

Georgiev, S.V. et al., 2019. Comprehensive evolution of a petroleum system in absolute time: The example of Brynhild, Norwegian North Sea. Chemical Geology, 522: 260-282.

Gramlich, J.W., Murphy, T.J., Garner, E.L., Shields, W.R., 1973. Absolute isotopic abundance ratio and atomic weight of a reference sample of rhenium. Journal of Research of the National Bureau of Standards - A. Physics and Chemistry, 77A(6): 691-698.

Gu, X., Li, B., Fu, S., Xu, S., Dong, S., 2007a. Physicochemical properities of hydrocarbon-bearing fluids in the Youjiang Basin, South China. Bulletin of Mineralogy Petrology and Geochemistry, 26(3): 214-217.

Gu, X., Li, B., Xu, S., Fu, S., Dong, S., 2007b. Characteristics of hydrocarbons bearing ore forming fluids in the Youjiang Basin, South China: Implications for hydrocarbon accumulation and ore mineralization Earth Science Froniters, 14(5): 133-146.

Gu, X. et al., 2010. The coupling relationship between metallization and hydrocarbon accumulation in sedimentaty basins. Earth Science Frontiers, 17(2): 83-105.

Gu, X. et al., 2013. The genetic relationship between Carlin-type gold deposits and paleo-petroleum reservoirs in SW Guizhou, China: Evidence from organic petrography. Earth Science Froniters, 20(1): 92-106.

Gu, X.X. et al., 2012. Hydrocarbon- and ore-bearing basinal fluids: A possible link between gold mineralization and hydrocarbon accumulation in the Youjiang Basin, South China. Mineralium Deposita, 47(6): 663-682.

Hao, F. et al., 2015. The fate of CO_2 derived from thermochemical sulfate reduction (TSR) and effect of TSR on carbonate porosity and permeability, Sichuan Basin, China. Earth-Science Reviews, 141: 154-177.

Hausen, D.M., 2000. Characterizing the textural features of gold ores for optimizing gold extraction. JOM, 52(4): 14-16.

Hnatyshin, D. et al., 2020. Understanding the microscale spatial distribution and mineralogical residency of Re in pyrite: Examples from carbonate-hosted Zn-Pb ores and implications for pyrite Re-Os geochronology. Chemical Geology, 533: 119427.

Hnatyshin, D., Creaser, R.A., Wilkinson, J.J., Gleeson, S.A., 2015. Re-Os dating of pyrite confirms an early diagenetic onset and extended duration of mineralization in the Irish Zn-Pb ore field. Geology, 43(2): 143-146.

Hofstra, A.H., Cline, J.S., 2000. Characteristics and models for Carlin-type gold deposits. Reviews in Economic Geology, 13: 163-220.

Hu, R., Su, W., Bi, X., Li, Z., 1995. A possible evolution way of ore-formation hydrothermal fluid for the Carlin-type gold deposit in the Yunnan-Guizhou-Guangxi triangle area. Acta Mineralogica Sinica, 15(2): 144-149.

Hu, R.Z., Su, W.C., Bi, X.W., Tu, G.Z., Hofstra, A.H., 2002. Geology and geochemistry of Carlin-type gold deposits in China. Mineralium Deposita, 37(3-4): 378-392.

Hu, S., He, L., Wang, J., 2000. Heat flow in the continental area of China: a new data set. Earth and Planetary Science Letters, 179(2): 407-419.

Hulen, J.B., Collister, J.W., 1999. The oil-bearing, Carlin-type gold deposits of Yankee Basin, Alligator Ridge district, Nevada. Economic Geology, 94(7): 1029-1049.

Hulen, J.B., Collister, J.W., Stout, B., Curtiss, D.K., Dahdah, N.F., 1998. The exhumed "Carlin-type" fossil oil reservoir at Yankee Basin. JOM, 50(12): 30-34.

Jaireth, S., McKay, A., Lambert, I., 2008. Association of large sandstone uranium deposits with hydrocarbons. AusGeo News, 89(6): 1-6.

Jin, X., 2017. Geology, mineralization and genesis of the Nibao, Shuiyindong and Yata gold deposits in SW Guizhou Province, China, China University of Geoscience, Wuhan, 208 pp.

Jin, X. et al., 2016. Relationship between Carlin-type gold deposits and paleopetroleum reservoirs in SW Guizhou, China: Evidence from gas compositions of fluid inclusions and Raman spectroscopic characteristics of bitumen. Acta Petrologica Sinica, 32(11): 3295-3311.

Kelley, K.D., Selby, D., Falck, H., Slack, J.F., 2017. Re-Os systematics and age of pyrite associated with stratiform Zn-Pb mineralization in the Howards Pass district, Yukon and Northwest Territories, Canada. Mineralium Deposita, 52(3): 317-335.

Kendall, B., Creaser, R.A., Selby, D., 2009. ^{187}Re-^{187}Os geochronology of Precambrian organic-rich sedimentary rocks. Geological Society of London, Special Publications, 326(1): 85-107.

Kesler, S.E. et al., 1994. Role of crude oil in the genesis of Mississippi Valley-type deposits: Evidence from the Cincinnati arch. Geology, 22(7): 609-612.

Kribek, B., Zak, K., Spangenberg, J.E., Jehlicka, J., Kominek, J., 1999. Bitumens in the late Variscan hydrothermal vein-type uranium deposit of Pribram, Czech Republic: Sources, radiation-induced alteration, and relation to mineralization. Economic Geology, 94(7): 1093-1114.

Lai, C.-K. et al., 2014. The western Ailaoshan volcanic belts and their SE Asia connection: A new tectonic model for the Eastern Indochina Block. Gondwana Research, 26(1): 52-74.

Large, R.R., Bull, S.W., Maslennikov, V.V., 2011. A carbonaceous sedimentary source-rock model for Carlin-type and orogenic gold deposits. Economic Geology, 106(3): 331-358.

Large, S.J.E. et al., 2016. Trace elements in fluid inclusions of sediment-hosted gold deposits indicate a magmatic-hydrothermal origin of the Carlin ore trend. Geology, 44(12): 1015-1018.

Lawley, C., Selby, D., Imber, J., 2013. Re-Os molybdenite, pyrite, and chalcopyrite geochronology, Lupa Goldfield, southwestern Tanzania: Tracing metallogenic time scales at midcrustal shear zones hosting orogenic Au deposits. Economic Geology, 108(7): 1591-1613.

Lewan, M., 1985. Evaluation of petroleum generation by hydrous pyrolysis experimentation. Philosophical Transactions of the Royal Society of London. Series A, Mathematical and Physical Sciences, 315(1531): 123-134.

Li, Z. et al., 2017. Rhenium-osmium geochronology in dating petroleum systems: progress and chanllenges. Acta Petrolei Sinica, 38(3): 297-306.

Lillis, P.G., Selby, D., 2013. Evaluation of the rhenium–osmium geochronometer in the Phosphoria petroleum system, Bighorn Basin of Wyoming and Montana, USA. Geochimica et Cosmochimica Acta, 118: 312-330.

Liu, J., Selby, D., 2017. A matrix matched reference material for validating petroleum Re-Os measurements. Geostandards and Geoanalytical Research., 42(1): 97-113.

Liu, J., Selby, D., Obermajer, M., Mort, A., 2018. Re-Os geochronology and oil-source correlation of Duvernay petroleum system, western Canada sedimentary basin: Implications for the application of the Re-Os geochronometer to petroleum systems. AAPG Bulletin, 108(8): 1627-1657.

Liu, J., Ye, J., Liu, J., Jun, T., Niu, J., 2000. Oil accumulation and ore formation. Bulletin of Mineralogy Petrology and Geochemistry, 19(3): 164-171.

Liu, T., Liu, B., Chen, G., Wu, Z., 2001. Tectonic evolution and hydrocarbon preservation region dividion in Nanpanjiang Basin. Natural Gas Industry, 21(1): 18-23.

Liu, Y., Hu, K., Han, S., Sun, Z., 2016. The characteristics of organic matter and its relationship with the formation of Carlin-type gold deposits in southwest Guizhou Province. Geochimica, 45(3): 281-302.

Ludwig, K., 2008. User's manual for Isoplot 3.7: A geochronological toolkit for Microsoft Excel: Berkeley, California, Berkeley Geochronology Center, Special Publication No.4, 76 pp.

Machel, H.G., 2001. Bacterial and thermochemical sulfate reduction in diagenetic settings - Old and new insights. Sedimentary Geology, 140(1–2): 143-175.

Machel, H.G., Krouse, H.R., Sassen, R., 1995. Products and distinguishing criteria of bacterial and thermochemical sulfate reduction. Applied Geochemistry, 10(4): 373-389.

Mastalerz, M., Bustin, R.M., Sinclair, A.J., Stankiewicz, B.A., 1995. Carbon-rich material in the Erickson hydrothermal system, northern British Columbia, Canada; origin and formation mechanisms. Economic Geology, 90(4): 938-947.

Migdisov, A. et al., 2017. Hydrocarbons as ore fluids. Geochemical Perspectives Letters, 5: 47-52.

Mirasol-Robert, A. et al., 2017. Evidence and origin of different types of sedimentary organic matter from a Paleoproterozoic orogenic Au deposit. Precambrian Research, 299: 319-338.

Mossman, D.J., Nagy, B., Davis, D.W., 1993. Comparative Molecular, Elemental, and U-Pb Isotopic Composition of Stratiform and Dispersed-Globular Matter in the Paleoproterozoic Uraniferous Metasediments, Elliot Lake, Canada. Energy Sources, 15(2): 377-387.

Muntean, J.L., 2018a. The Carlin gold system: Applications to exploration in Nevada and beyond. In: Muntean, J.L. (Ed.), Diversity in Carlin-style gold deposits. Society of Economic Geologists Special Publications, v. 20, pp. 39-88.

Muntean, J.L., 2018b. Diversity of Carlin-style gold deposits. In: Muntean, J.L. (Ed.), Diversity in Carlin-style gold deposits. Society of Economic Geologists Special Publications, v. 20, pp. 1-5.

Muntean, J.L., Cline, J.S., Simon, A.C., Longo, A.A., 2011. Magmatic–hydrothermal origin of Nevada's Carlin-type gold deposits. Nature Geoscience, 4(2): 122-127.

Nakai, S.I. et al., 1993. Rb-Sr dating of sphalerites from Mississippi Valley-type (MVT) ore deposits. Geochimica et Cosmochimica Acta, 57(2): 417-427.

Nutt, C.J., Hofstra, A.H., 2003. Alligator Ridge district, east-central Nevada: Carlin-type gold mineralization at shallow depths. Economic Geology, 98(6): 1225-1241.

Pan, C., Yu, L., Liu, J., Fu, J., 2006. Chemical and carbon isotopic fractionations of gaseous hydrocarbons during abiogenic oxidation. Earth and Planetary Science Letters, 246(1): 70-89.

Parnell, J., 1994. Geofluids: Origin, migration and evolution of fluids in sedimentary basins:Geological Society of London, Special Publications, 78, 374 pp.

Parnell, J., McCready, A., 2000. Paragenesis of gold- and hydrocarbon-bearing fluids in gold deposits, Organic Matter and Mineralisation: Thermal Alteration, Hydrocarbon Generation and Role in Metallogenesis. Springer, pp. 38-52.

Pearcy, E.C., Burruss, R.C., 1993. Hydrocarbons and Gold Mineralization in the Hot-Spring Deposit at Cherry Hill, California. In: Parnell, J., Kucha, H., Landais, P. (Eds.), Bitumens in Ore Deposits. Springer Berlin Heidelberg, Berlin, Heidelberg, pp. 117-137.

Peters, K., Walters, C., Moldowan, J., 2005. The biomarker guide, biomarkers and isotopes in Petroleum exploration and Earth history: New York, 1-2. Cambridge University Press, 961 pp.

Peucker‐Ehrenbrink, B., Jahn, B.m., 2001. Rhenium‐osmium isotope systematics and platinum group element concentrations: Loess and the upper continental crust. Geochemistry, Geophysics, Geosystems, 2(10): 2001GC000172.

Pi, Q., Hu, R., Xiong, B., Li, Q., Zhong, R., 2017. In situ SIMS U-Pb dating of hydrothermal rutile: Reliable age for the Zhesang Carlin-type gold deposit in the golden triangle region, SW China. Mineralium Deposita, 52(8): 1179-1190.

Powell, T.G., Macqueen, R.W., 1984. Precipitation of Sulfide Ores and Organic Matter: Sulfate Reactions at Pine Point, Canada. Science, 224(4644): 63-6.

Qin, J., Wu, Y., Yan, Y., Zhu, Z., 1996. Hercynian-Indosinian sedimentary-tectonic evolution of the Nanpanjiang Basin. Acta Geologica Sinica, 70(2): 99-107.

Robb, L.J., Meyer, F.M., 1995. The Witwatersrand Basin, South Africa: Geological framework and mineralization processes. Ore Geology Reviews, 10(2): 67-94.

Saintilan, N.J., Selby, D., Creaser, R.A., Dewaele, S., 2018. Sulphide Re-Os geochronology links orogenesis, salt and Cu-Co ores in the Central African Copperbelt. Scientific Reports, 8(1): 14946.

Saintilan, N.J. et al., 2019. Petroleum as source and carrier of metals in epigenetic sediment-hosted mineralization. Science Reports, 9(1): 8283.

Seal, R.R., II, 2006. Sulfur Isotope Geochemistry of Sulfide Minerals. Reviews in Mineralogy and Geochemistry, 61(1): 633-677.

Seifert, W., Moldowan, J., 1986. Use of biological markers in petroleum exploration. Methods in Geochemistry and Geophysics, 24: 261-290.

Selby, D., Creaser, R.A., 2005. Direct radiometric dating of hydrocarbon deposits using rhenium-osmium isotopes. Science, 308(5726): 1293-1295.

Selby, D., Creaser, R.A., Dewing, K., Fowler, M., 2005. Evaluation of bitumen as a ^{187}Re–^{187}Os geochronometer for hydrocarbon maturation and migration: A test case from the Polaris MVT deposit, Canada. Earth and Planetary Science Letters, 235(1): 1-15.

Selby, D., Kelley, K.D., Hitzman, M.W., Zieg, J., 2009. Re–Os sulfide (bornite, chalcopyrite, and pyrite) systematics of the carbonate-hosted copper deposits at Ruby Creek, southern Brooks Range, Alaska. Economic Geology, 104(3): 437-444.

Shi, C. et al., 2020. Hydrocarbon evolution of the over-mature Sinian Dengying reservoir of the Neoproterozoic Sichuan Basin, China: Insights from Re–Os geochronology. Marine and Petroleum Geology, 122: 104726.

Shirey, S.B., Walker, R.J., 1995. Carius tube digestion for low-blank rhenium-osmium analysis. Analytical Chemistry, 67(13): 2136-2141.

Smoliar, M.I., Walker, R.J., Morgan, J.W., 1996. Re-Os ages of group IIA, IIIA, IVA, and IVB iron meteorites. Science, 271(5252): 1099-1102.

Stein, H.J., Morgan, J.W., Anders, S., 2000. Re-Os dating of low-level highly radiogenic (LLHR) sulfides: The Harnas gold deposit, douthwest Sweden, records continental-scale tectonic events. Economic Geology, 95(8): 1657-1671.

Su, W. et al., 2018. Carlin-type gold deposits in the Dian-Qian-Gui “golden triangle” of southwest China. In: Muntean, J.L. (Ed.), Diversity in Carlin-style gold deposits. Society of Economic Geologists Special Publications, v. 20, pp. 157-185.

Su, W., Hu, R., Xia, B., Xia, Y., Liu, Y., 2009. Calcite Sm-Nd isochron age of the Shuiyindong Carlin-type gold deposit, Guizhou, China. Chemical Geology, 258(3): 269-274.

Su, W. et al., 2012. Mineralogy and geochemistry of gold-bearing arsenian pyrite from the Shuiyindong Carlin-type gold deposit, Guizhou, China: Implications for gold depositional processes. Mineralium Deposita, 47(6): 653-662.

Tan, Q.-P., Xia, Y., Xie, Z.-J., Yan, J., 2015. Migration paths and precipitation mechanisms of ore-forming fluids at the Shuiyindong Carlin-type gold deposit, Guizhou, China. Ore Geology Reviews, 69: 140-156.

Thomson, M.L., Mastalerz, M., Sinclair, A.J., Bustin, R.M., 1992. Fluid source and thermal history of an epithermal vein deposit, Owen Lake, central British Columbia: evidence from bitumen and fluid inclusions. Mineralium Deposita, 27(3): 219-225.

Völkening, J., Walczyk, T., Heumann, K.G., 1991. Osmium isotope ratio determinations by negative thermal ionization mass spectrometry. International Journal of Mass Spectrometry and Ion Processes, 105(2): 147-159.

Wang, G., 1992. Three stronitum and rubidium isotime ages in northwest Guangxi. Geology of Guangxi, 5(1): 29-35.
Wells, J.D., Mullens, T.E., 1973. Gold-bearing arsenian pyrite determined by microprobe analysis, Cortez and Carlin gold mines, Nevada. Economic Geology, 68(2): 187-201.
Williams-Jones, A.E., Bowell, R.J., Migdisov, A.A., 2009. Gold in Solution. Elements, 5(5): 281-287.
Wilson, N.S.F., Zentilli, M., 2006. Association of pyrobitumen with copper mineralization from the Uchumi and Talcuna districts, central Chile. International Journal of Coal Geology, 65(1): 158-169.
Worden, R.H., Smalley, P.C., 1996. H_2S-producing reactions in deep carbonate gas reservoirs: Khuff Formation, Abu Dhabi. Chemical Geology, 133(1): 157-171.
Wu, C., 2012. Organic matter in Carlin-type gold deposits and paleo-oil reservoirs in southwest Guizhou - Source, maturity and association, China University of Geosciences, Beijing, 91 pp.
Wu, Y.-F. et al., 2020. Distribution of trace elements between carbonaceous matter and sulfides in a sediment-hosted orogenic gold system. Geochimica et Cosmochimica Acta, 276: 345-362.
Xie, Z. et al., 2018a. Are there Carlin-type gold deposits in China? A comparison of the Guizhou, China, deposits with Nevada, USA, deposits. In: Muntean, J.L. (Ed.), Diversity in Carlin-style gold deposits. Society of Economic Geologists Special Publications, v. 20, pp. 187-233.
Xie, Z. et al., 2018b. Magmatic Origin for Sediment-Hosted Au Deposits, Guizhou Province, China: In Situ Chemistry and Sulfur Isotope Composition of Pyrites, Shuiyindong and Jinfeng Deposits. Economic Geology, 113(7): 1627-1652.
Xiong, S.-F. et al., 2019. Gold distribution and source of the J4 gold-bearing breccia pipe in the Qiyugou district, North China Craton: Constraints from ore mineralogy and in situ analysis of trace elements and S-Pb isotopes. Ore Geology Reviews, 105: 514-536.
Yan, J. et al., 2018. NanoSIMS element mapping and sulfur isotope analysis of Au-bearing pyrite from Lannigou Carlin-type Au deposit in SW China: New insights into the origin and evolution of Au-bearing fluids. Ore Geology Reviews, 92: 29-41.
Zaw, K. et al., 2014. Tectonics and metallogeny of mainland Southeast Asia — A review and contribution. Gondwana Research, 26(1): 5-30.
Zhang, R.-X., Yang, S.-Y., 2016. A Mathematical Model for Determining Carbon Coating Thickness and Its Application in Electron Probe Microanalysis. Microscopy and Microanalysis, 22(6): 1374-1380.
Zhang, X.-C., Spiro, B., Halls, C., Stanley, C.J., Yang, K.-Y., 2003. Sediment-hosted disseminated gold deposits in southwest Guizhou, PRC: Their geological setting and origin in relation to mineralogical, fluid inclusion, and stable-isotope characteristics. International Geology Review, 45(5): 407-470.
Zhang, X., 1997. The geology and hydrothermal evolution of sediment-hosted gold deposits in Southwestern Guzhou Province, PRC: Unpublished Ph.D. Thesis, Imperial College of London, 273 pp.
Zhao, M., Zhang, S., Zhao, L., Liu, P., 2006a. Oil and gas accumulation and gas exploration potential in the Nanpanjiang Basin, China. Geological Review, 52(5): 642-649.
Zhao, M., Zhang, S., Zhao, L., Liu, P., 2006b. The thermal evolution history and oil and gas generation history of main source rocks in the Nanpanjiang Basin. Petroeum Geology & Experiment, 28(3): 271-275.

Zhao, M., Zhang, S., Zhao, L., Liu, P., Da, J., 2007. Geochemical characteristics and genesis of the bitumen and gas in the Palaeo-reservoirs, Nanpanjiang Basin. Science in China Series D: Earth Sciences, 37(2): 167-177.

Zhao, M., Zhao, L., Zhang, S., Liu, P., 2006c. Geochemical characteristics of main source rocks in the Nanpanjiang Basin. Petroleum Geology & Experiment, 28(2): 162-167.

Zhou, M., 1999. A study on the pereoleum system of Nanpanjiang Sag. Yunnan Geology, 18(3): 248-265.

Zhu, G., Zhang, S., Liang, Y., Dai, J., Li, J., 2005. Isotope evidence for the TSR genesis high H2S natural gas of the Feixianguan Formation, northeast Sichuan Basin. Science in China Series D: Earth Sciences, 35(11): 1037-1046.

Zhu, G. et al., 2013. Alteration and multi-stage accumulation of oil and gas in the Ordovician of the Tabei uplift, Tarim Basin, NW China: implications for genetic origin of the diverse hydrocarbons. Marine and Petroleum Geology, 46: 234-250.

Zhu, J., Zhang, Z., Santosh, M., Jin, Z., 2020. Carlin-style gold province linked to the extinct Emeishan plume. Earth and Planetary Science Letters, 530: 115940.

Zhuang, H., Lu, J., Fu, J., Liu, D., 2000. Organic petrological study on solid organic matter in two Carlin-type gold deposits in the southwest Guizhou, China Scientia Geologica Sinica, 35(1): 83-90.

Zhuang, H., Lu, J., Fu, J., Ren, C., Zou, D., 1998. Crude oil as a carrier of gold migration: possible petrological and geochemical evidence. Science in China Series D: Earth Sciences, 28(6): 552-558.

Zimmerman, A., Stein, H.J., Morgan, J.W., Markey, R.J., Watanabe, Y., 2014. Re–Os geochronology of the El Salvador porphyry Cu–Mo deposit, Chile: Tracking analytical improvements in accuracy and precision over the past decade. Geochimica et Cosmochimica Acta, 131: 13-32.

Figure Captions

Figure 1: Simplified geological map of Nanpanjiang Basin, South China block. (A) Tectonic location map of Nanpanjiang Basin. (B) Simplified geological and structural map of Nanpanjiang Basin, showing locations of both hydrocarbon reservoir and gold deposits. F1: Mile-Shizong faults, F2: Ziyun-Du’an fault, F3: Napou-Funing fault, F4: Pingxiang-Nanning fault, F5: Youjiang fault, F6: Poping thrust.

Figure 2: Comprehensive stratigraphic column of Nanpanjiang Basin showing hydrocarbon systems, gold deposits, and associated tectonic events.

Figure 3: Geological map of Laizishan–Yata–Banqi area showing sample locations of pyrobitumen and pyrite analyzed in this study.

Figure 4: Typical outcrop, reflected light images and BSE images of pyrobitumen and pyrite samples from Laizishan (LZS) and Banqi (BQ) reservoirs, and Yata (YT) gold deposit analyzed in this study. (a) Pyrobitumen associating with calcite from the Permian Wujiaping Formation, Laizishan reservoir. (b) Typical reflected light images of the calcite, pyrobitumen and pyrite in the Laizishan reservoir with pyrobitumen and pyrite together present in pore spaces between calcite grains. (c) Pyrobitumen and associated calcite in the Permian Wujiaping Limestome, Banqi reservoir. (d) Typical reflected light images in the Banqi reservoir showing pyrobitumen and pyrite together distributed along the boundary of calcite grains. (e) Disseminated pyrite hosted in siltstone of the Middle Triassic Xinyuan Formation, Yata deposit. (f) Typical reflected light images showing shape and distribution of pyrite grains in the Yata deposit. (g) backscattered electron (BSE) image showing the feature of pyrite grains (YT-31) in the Yata deposit. (h) backscattered electron (BSE) image showing the rim-core structure of the pyrite (YT-43) with rim contains higher Au than the core. The yellow points in g and h are the EPMA locations. Mineral abbreviations: Py – pyrite, Cal – calcite, Bt – pyrobitumen

Figure 5: Traditional $^{187}Re/^{188}Os$ vs. $^{187}Os/^{188}Os$ plot showing all Re-Os pyrobitumen data from Laizishan and Banqi reservoirs. Data labels are sample numbers listed in Table 1. MSWD = mean square weighted deviation. See text for discussion.

Figure 6: Traditional $^{187}Re/^{188}Os$ vs. $^{187}Os/^{188}Os$ plot showing Re-Os data for all pyrite samples from Yata (YT) gold deposit. Data labels are sample numbers listed in Table 2. MSWD = mean square weighted deviation. See text for discussion.

Figure 7: Basin modeling of strata in Yang-1 well in Nanpanjiang Basin, showing key interval of petroleum evolution (modified from Zhao et al., 2006).

Figure 8: Compiled chronology and mineral formation sequence in Nanpanjiang Basin. Cited references are (1) Hu et al., 1995; (2) Jin, 2017; (3) Wang, 1992; (4) Chen et al.,2015; (5) Pi et al., 2017; (6) Chen et al., 2009; (7) Gu et al., 2012; (8) Su et al., 2009.

Figure 9: Simplified model for relationship between hydrocarbon evolution and Carlin-type gold deposits in Nanpanjiang Basin

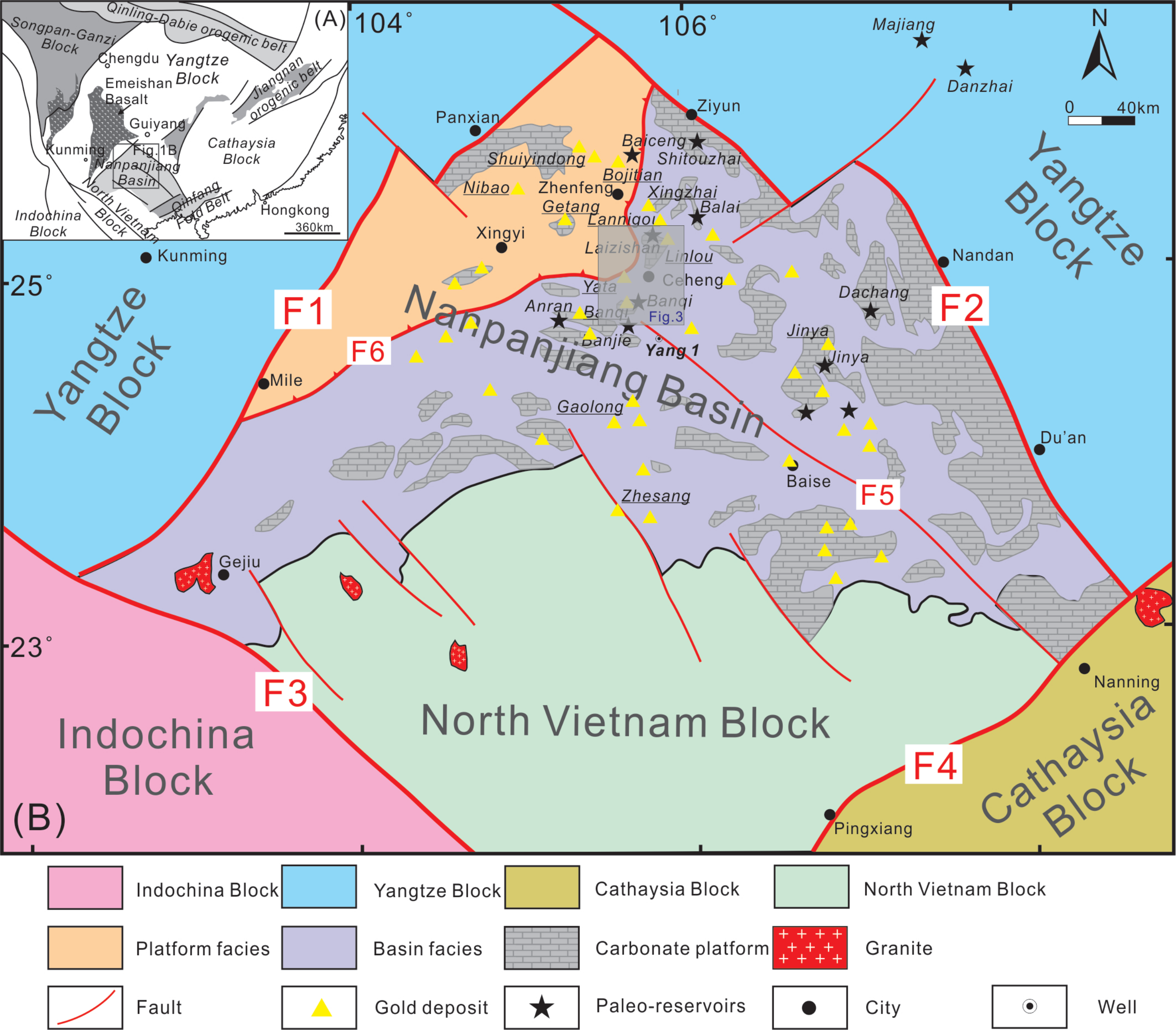
(A)
Songpan-Ganzi Block
Qinling-Dabie orogenic belt
Chengdu
Yangtze Block
Emeishan Basalt
Jiangnan orogenic belt
Guiyang
Kunming
Fig.1B
Nanpanjiang Basin
Cathaysia Block
North Vietnam Block
Qinfang Fold Belt
Indochina Block
Hongkong
360km
(B)
104°
106°
25°
23°
N
0 40km
Majiang
Danzhai
Panxian
Ziyun
Baiceng
Shitouzhai
Shuiyindong
Bojitian
Nibao
Zhenfeng
Xingzhai
Getang
Balai
Lannigou
Xingyi
Laizishan
Linlou
Kunming
Nandan
Ceheng
Yata
Banqi
Dachang
Anran
Banqi
Fig.3
Banjie
Yang 1
Jinya
Jinya
F1
F2
F6
Nanpanjiang Basin
Yangtze Block
Yangtze Block
Mile
Gaolong
Du'an
Baise
F5
Zhesang
Gejiu
F3
Nanning
North Vietnam Block
Indochina Block
F4
Cathaysia Block
Pingxiang
Indochina Block
Yangtze Block
Cathaysia Block
North Vietnam Block
Platform facies
Basin facies
Carbonate platform
Granite
Fault
Gold deposit
Paleo-reservoirs
City
Well

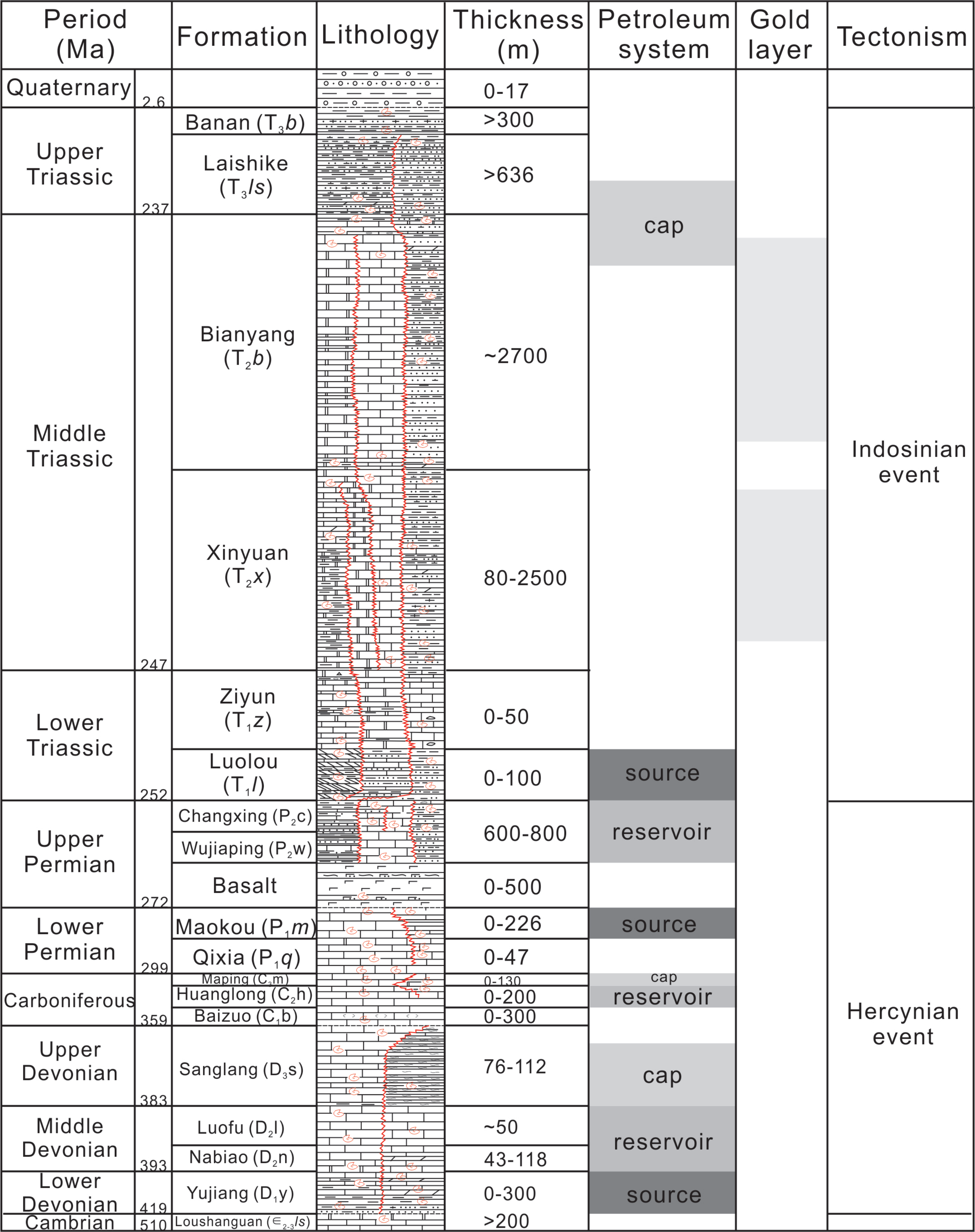

Period (Ma)
Formation
Lithology
Thickness (m)
Petroleum system
Gold layer
Tectonism
Quaternary
2.6
0-17
Upper Triassic
Banan (T_3b)
>300
Laishike (T_3ls)
>636
237
Middle Triassic
Bianyang (T_2b)
~2700
cap
Xinyuan (T_2x)
80-2500
247
Indosinian event
Lower Triassic
Ziyun (T_1z)
0-50
Luolou (T_1l)
0-100
source
252
Upper Permian
Changxing (P_2c)
Wujiaping (P_2w)
600-800
reservoir
Basalt
0-500
272
Lower Permian
Maokou (P_1m)
0-226
source
Qixia (P_1q)
0-47
299
Carboniferous
Maping (C_3m)
0-130
cap
Huanglong (C_2h)
0-200
reservoir
Baizuo (C_1b)
0-300
359
Upper Devonian
Sanglang (D_3s)
76-112
cap
383
Middle Devonian
Luofu (D_2l)
~50
reservoir
Nabiao (D_2n)
43-118
393
Lower Devonian
Yujiang (D_1y)
0-300
source
419
Cambrian
Loushanguan ($\in_{2-3}ls$)
>200
510
Hercynian event

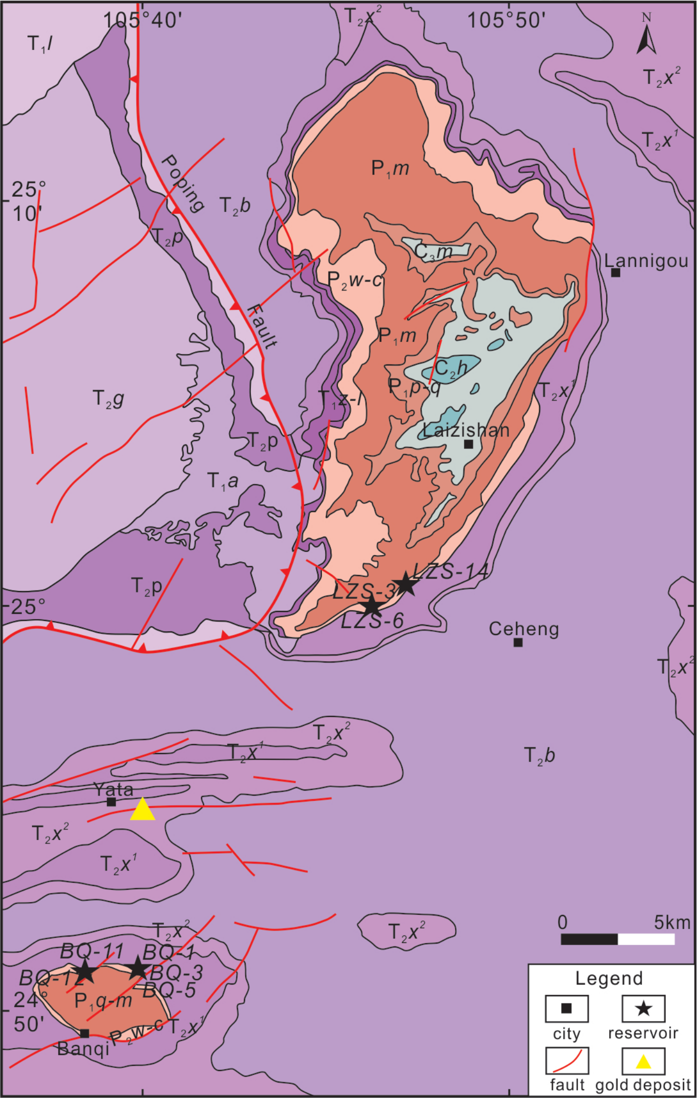

105°40'
105°50'
N
T_1l
T_2x^2
T_2x^1
25° 10'
Poping Fault
T_2b
T_2p
P_1m
C_3m
$P_2w\text{-}c$
Lannigou
T_2g
C_2h
$P_1p\text{-}q$
$T_1z\text{-}l$
Laizishan
T_1a
LZS-14
LZS-3
LZS-6
25°
Ceheng
Yata
T_2b
0
5km
BQ-11
BQ-1
BQ-12
BQ-3
BQ-5
24° 50'
$P_1q\text{-}m$
$P_2w\text{-}c$
Banqi
Legend
city
reservoir
fault
gold deposit

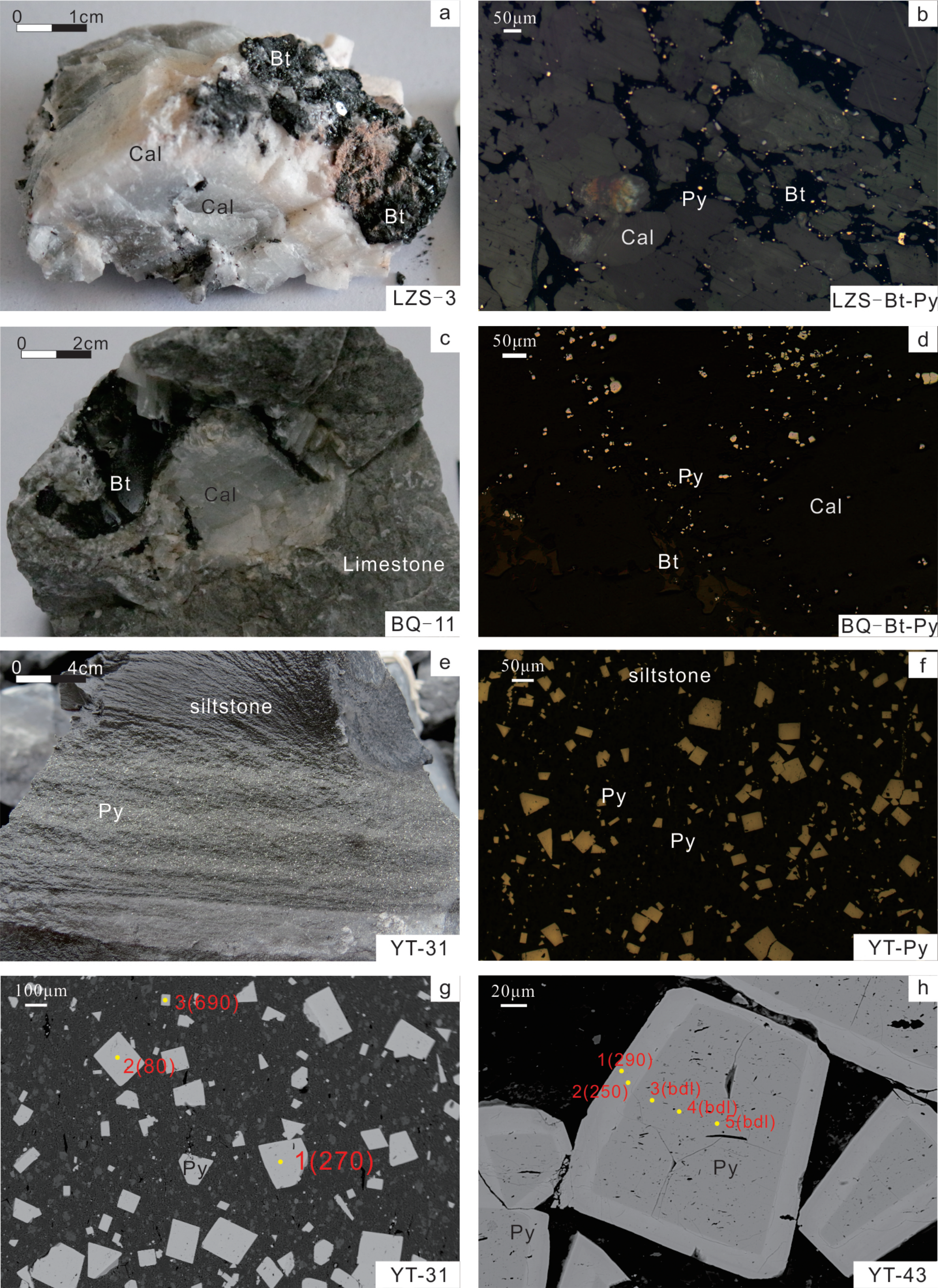

0 1cm
a
Bt
Cal
Cal
Bt
LZS-3
50μm
b
Py
Bt
Cal
LZS-Bt-Py
0 2cm
c
Bt
Cal
Limestone
BQ-11
50μm
d
Py
Cal
Bt
BQ-Bt-Py
0 4cm
e
siltstone
Py
YT-31
50μm
f
siltstone
Py
Py
YT-Py
100μm
g
3(690)
2(80)
1(270)
Py
YT-31
20μm
h
1(290)
2(250)
3(bdl)
4(bdl)
5(bdl)
Py
Py
YT-43

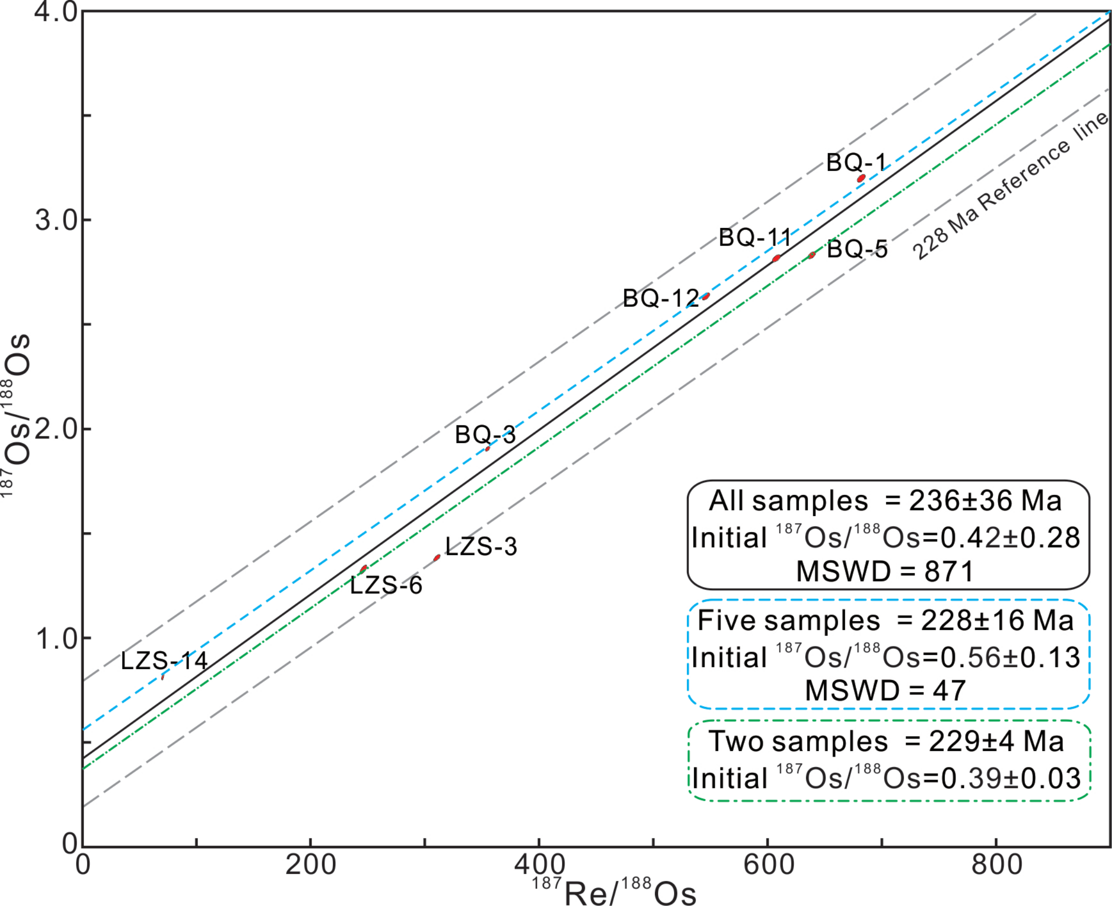

4.0
3.0
2.0
1.0
0
0
200
400
600
800
^{187}Os/^{188}Os
^{187}Re/^{188}Os
BQ-1
BQ-11
BQ-5
BQ-12
BQ-3
LZS-3
LZS-6
LZS-14
228 Ma Reference line
All samples = 236±36 Ma
Initial ^{187}Os/^{188}Os=0.42±0.28
MSWD = 871
Five samples = 228±16 Ma
Initial ^{187}Os/^{188}Os=0.56±0.13
MSWD = 47
Two samples = 229±4 Ma
Initial ^{187}Os/^{188}Os=0.39±0.03

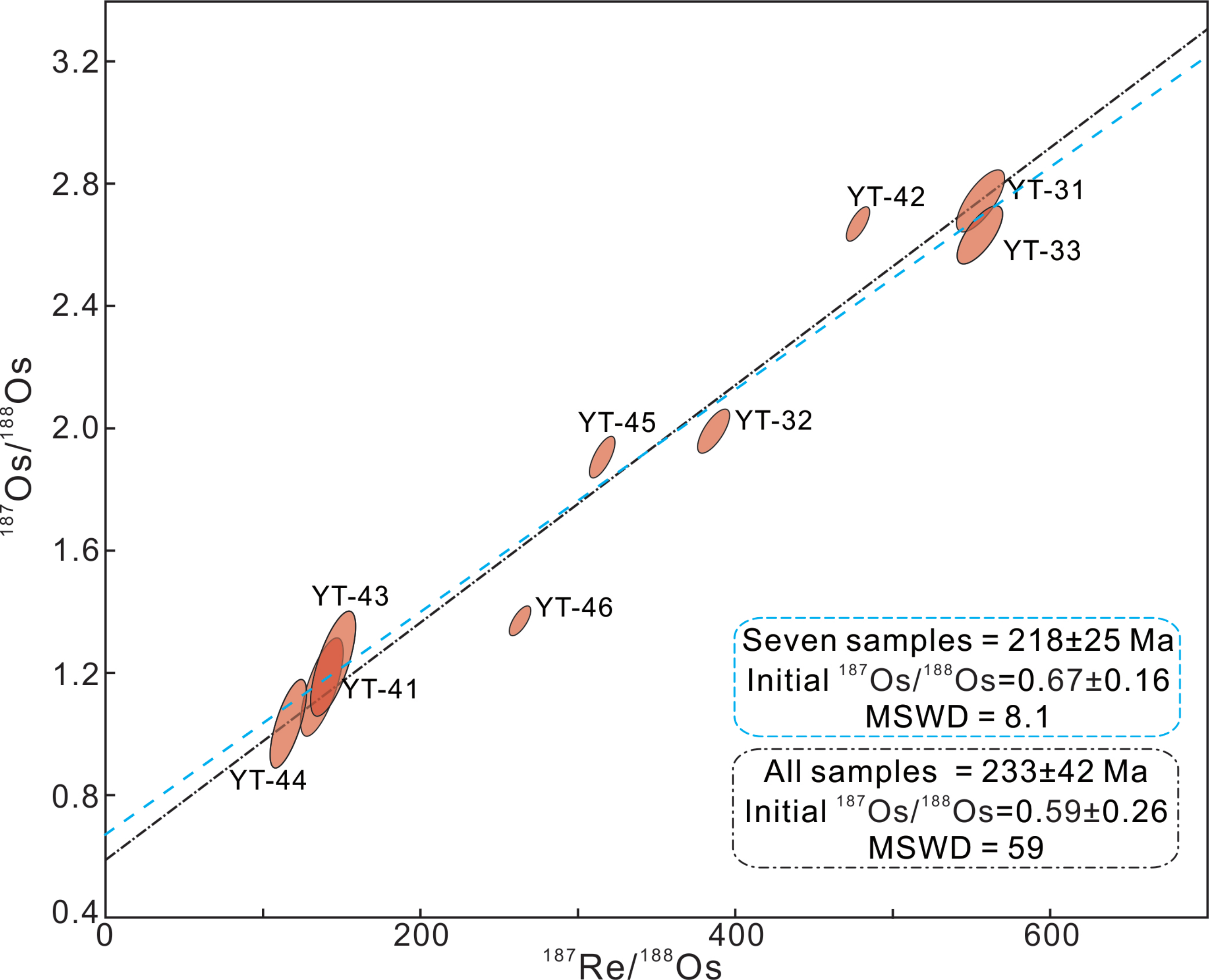

3.2
2.8
2.4
2.0
1.6
1.2
0.8
0.4
0
200
400
600
^{187}Os/^{188}Os
^{187}Re/^{188}Os
YT-42
YT-31
YT-33
YT-45
YT-32
YT-43
YT-46
YT-41
YT-44
Seven samples = 218±25 Ma
Initial ^{187}Os/^{188}Os=0.67±0.16
MSWD = 8.1
All samples = 233±42 Ma
Initial ^{187}Os/^{188}Os=0.59±0.26
MSWD = 59

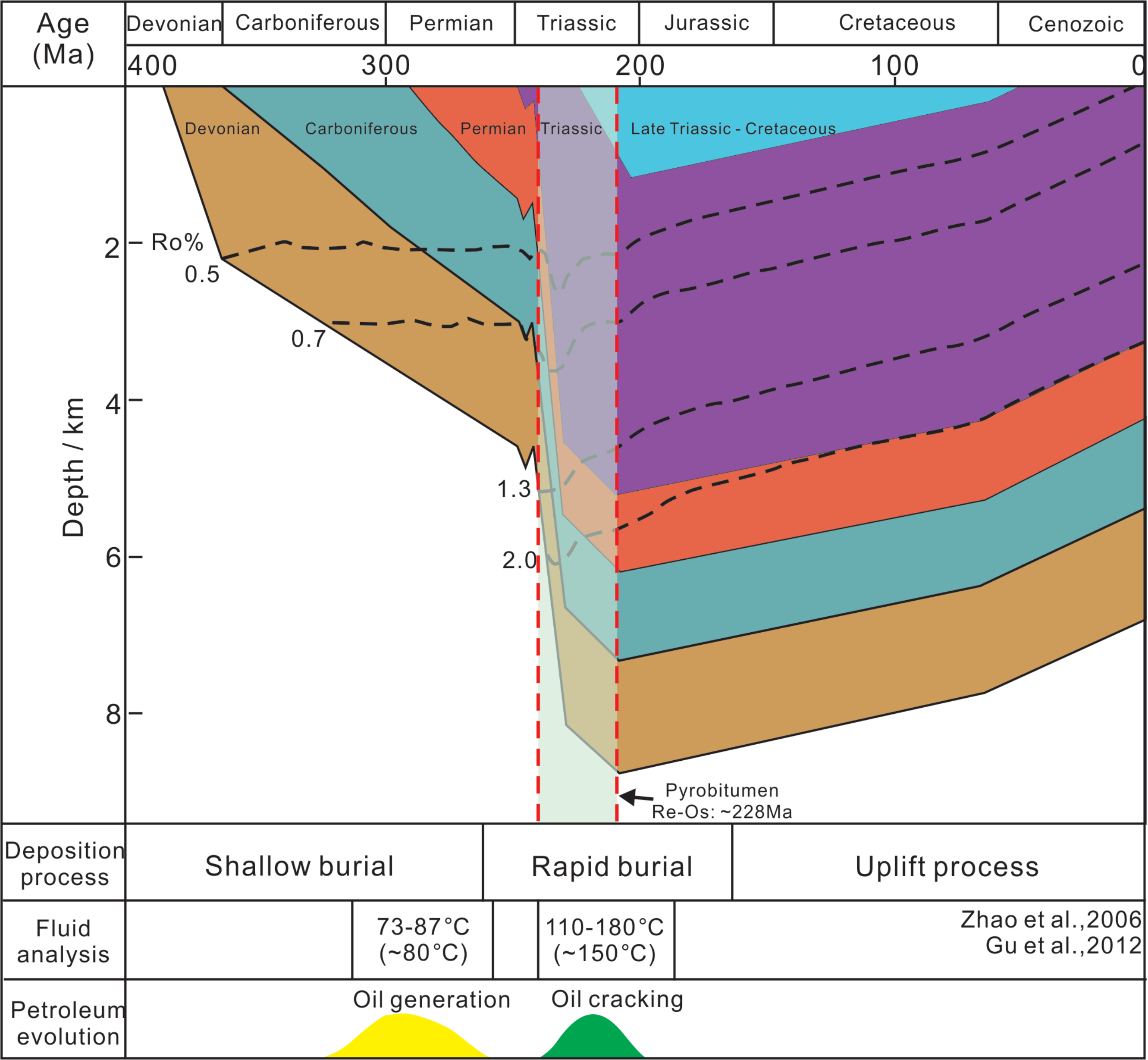

Age (Ma)
Devonian
Carboniferous
Permian
Triassic
Jurassic
Cretaceous
Cenozoic
400
300
200
100
0
Devonian
Carboniferous
Permian
Triassic
Late Triassic - Cretaceous
Ro%
0.5
0.7
1.3
2.0
2
4
6
8
Depth / km
Pyrobitumen
Re-Os: ~228Ma
Deposition process
Shallow burial
Rapid burial
Uplift process
Fluid analysis
73-87°C
(~80°C)
110-180°C
(~150°C)
Zhao et al.,2006
Gu et al.,2012
Petroleum evolution
Oil generation
Oil cracking

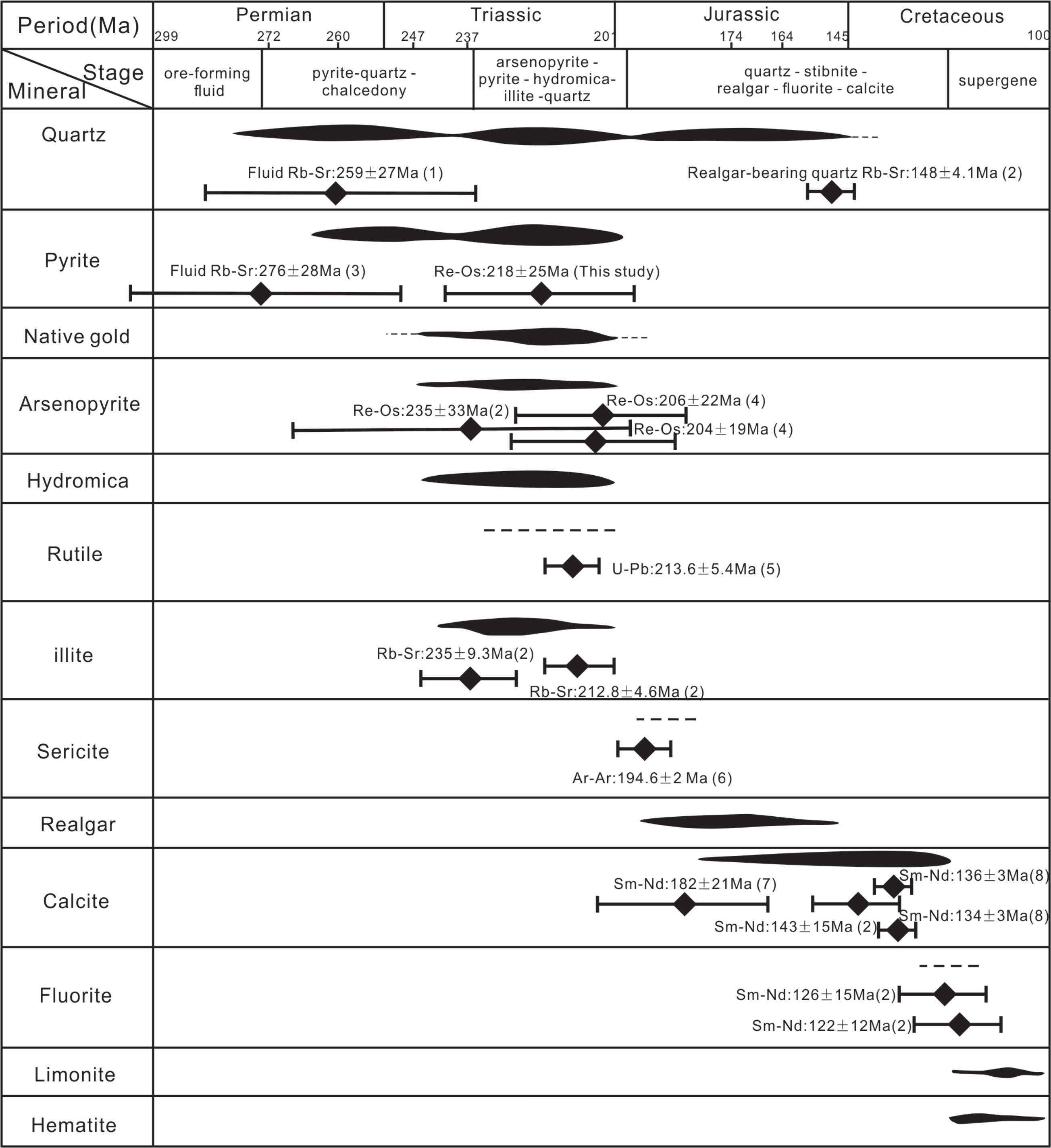
Period(Ma)
Permian
Triassic
Jurassic
Cretaceous
299
272
260
247
237
201
174
164
145
100
Stage
Mineral
ore-forming fluid
pyrite-quartz - chalcedony
arsenopyrite - pyrite - hydromica- illite -quartz
quartz - stibnite - realgar - fluorite - calcite
supergene
Quartz
Fluid Rb-Sr:259±27Ma (1)
Realgar-bearing quartz Rb-Sr:148±4.1Ma (2)
Pyrite
Fluid Rb-Sr:276±28Ma (3)
Re-Os:218±25Ma (This study)
Native gold
Arsenopyrite
Re-Os:206±22Ma (4)
Re-Os:235±33Ma(2)
Re-Os:204±19Ma (4)
Hydromica
Rutile
U-Pb:213.6±5.4Ma (5)
illite
Rb-Sr:235±9.3Ma(2)
Rb-Sr:212.8±4.6Ma (2)
Sericite
Ar-Ar:194.6±2 Ma (6)
Realgar
Calcite
Sm-Nd:136±3Ma(8)
Sm-Nd:182±21Ma (7)
Sm-Nd:134±3Ma(8)
Sm-Nd:143±15Ma (2)
Fluorite
Sm-Nd:126±15Ma(2)
Sm-Nd:122±12Ma(2)
Limonite
Hematite

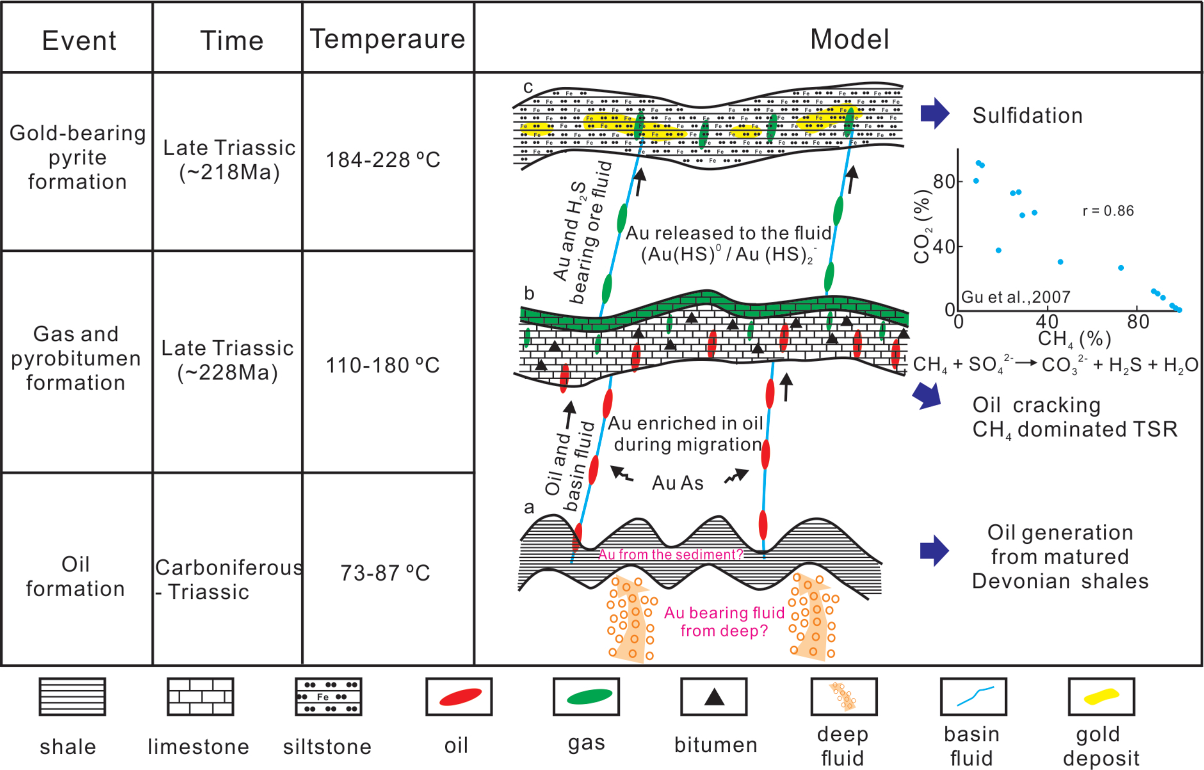

Event
Time
Temperaure
Model
Gold-bearing pyrite formation
Late Triassic (~218Ma)
184-228 °C
Gas and pyrobitumen formation
Late Triassic (~228Ma)
110-180 °C
Oil formation
Carboniferous - Triassic
73-87 °C
c
b
a
Au and H_2S bearing ore fluid
Au released to the fluid
$(Au(HS)^0$ / $Au(HS)_2^-$
Oil and basin fluid
Au enriched in oil during migration
Au As
Au from the sediment?
Au bearing fluid from deep?
Sulfidation
CO_2 (%)
CH_4 (%)
0
40
80
r = 0.86
Gu et al.,2007
$CH_4 + SO_4^{2-} \rightarrow CO_3^{2-} + H_2S + H_2O$
Oil cracking
CH_4 dominated TSR
Oil generation from matured Devonian shales
shale
limestone
siltstone
oil
gas
bitumen
deep fluid
basin fluid
gold deposit
Fe

Table 1. Rhenium–Osmium Elemental and Isotopic Data for Bitumen from Banqi and Laizishan reservoir, Nanpanjiang Basin

Sample	Latitude	Longitude	Formation	Re (ppb)	±	Os (ppt)	±	^{192}Os (ppt)	±	^{187}Os (ppt)	±	$^{187}Re/^{188}Os$	±	$^{187}Os/^{188}Os$	±	rho	Osi $_{236}$	±
BQ-1	24°51’35’’	105°40’21’’	Wujiaping	238.6	0.60	2360.6	12.7	695.1	2.4	704.8	2.4	683.0	2.9	3.209	0.015	0.571	0.52	0.03
BQ-3	24°51’35’’	105°40’21’’	Wujiaping	48.4	0.12	810.5	3.8	271.6	1.0	163.7	0.6	354.4	1.6	1.907	0.010	0.586	0.51	0.02
BQ-5	24°51’35’’	105°40’21’’	Wujiaping	175.4	0.44	1789.7	9.3	545.7	1.9	489.8	1.7	639.6	2.7	2.841	0.014	0.576	0.32	0.02
BQ-11	24°50’57’’	105°39’11’’	Wujiaping	101.4	0.26	1085.4	5.7	331.4	1.2	295.9	1.0	608.4	2.7	2.826	0.014	0.593	0.43	0.02
BQ-12	24°50’57’’	105°39’11’’	Wujiaping	140.7	0.38	1647	8.8	511.9	2.0	427.6	1.6	546.8	2.6	2.644	0.014	0.612	0.49	0.02
LZS-3	24°59’59’’	105°46’29’’	Wujiaping	11.6	0.03	209.2	1.3	74.2	0.5	32.5	0.2	309.9	2.3	1.386	0.013	0.702	0.17	0.02
LZS-6	24°59’59’’	105°46’29’’	Wujiaping	12.1	0.04	273.7	2.0	97.7	1.0	41.0	0.4	245.5	2.5	1.330	0.018	0.702	0.36	0.03
LZS-14	25°0’33’’	105°47’0’’	Wujiaping	5.2	0.02	405.5	2.5	153.5	1.4	40.0	0.4	67.6	0.7	0.824	0.010	0.642	0.56	0.01

Table 2. Rhenium–Osmium Elemental and Isotopic Data for pyrite from Yata gold deposit, Nanpanjiang Basin

Sample	Latitude	Longitude	Formation	Re (ppb)	±	Os (ppt)	±	^{192}Os (ppt)	±	^{187}Re/^{188}Os	±	^{187}Os/^{188}Os	±	rho	Osi_{233}	±
YT-31	24°54‘59‘‘	105°39’13’’	Xinyuan	3.26	0.01	37.9	0.6	11.6	0.3	556.5	12.5	2.75	0.08	0.729	0.59	0.13
YT-32	24°54‘59‘‘	105°39’13’’	Xinyuan	3.19	0.01	49.5	0.7	16.4	0.4	386.5	8.3	2.00	0.06	0.717	0.49	0.09
YT-33	24°54‘59‘‘	105°39’13’’	Xinyuan	4.67	0.01	53.7	0.8	16.7	0.4	556.3	11.9	2.64	0.08	0.717	0.48	0.12
YT-41	24°55‘01‘‘	105°39’12’’	Xinyuan	1.16	0.01	46.2	1.7	16.8	1.4	136.8	11.1	1.16	0.13	0.708	0.62	0.17
YT-42	24°55‘01‘‘	105°39’12’’	Xinyuan	7.89	0.02	105.8	1.1	32.8	0.4	478.7	6.0	2.68	0.05	0.703	0.81	0.07
YT-43	24°55‘01‘‘	105°39’12’’	Xinyuan	1.12	0.01	43.1	1.6	15.5	1.3	144.0	11.7	1.23	0.14	0.708	0.67	0.19
YT-44	24°55‘01‘‘	105°39’12’’	Xinyuan	0.63	0.01	29.6	1.1	10.9	0.9	115.5	9.4	1.04	0.12	0.708	0.59	0.15
YT-45	24°55‘01‘‘	105°39’12’’	Xinyuan	3.53	0.01	66.6	0.9	22.3	0.5	315.1	6.6	1.91	0.06	0.710	0.68	0.08
YT-46	24°55‘01‘‘	105°39’12’’	Xinyuan	3.94	0.02	84.0	1.1	29.8	0.6	262.8	5.6	1.37	0.04	0.693	0.35	0.06

Table 3. Electron Microprobe Analysis of gold bearing from the Yata deposit

Sample No.	mineral	Au (wt%)	As (wt%)	Fe (wt%)	S (wt%)	Ag (wt%)	Sb (wt%)	Zn (wt%)	Cu (wt%)	Total
YT-31	Pyrite	0.064	0.05	46.40	54.13	0.02	b.d.	b.d.	0.02	100.69
YT-31	Pyrite	0.030	0.06	46.39	54.14	b.d.	0.01	0.03	b.d.	100.67
YT-31	Pyrite	b.d.	0.08	46.09	53.67	0.01	b.d.	0.01	0.02	99.87
YT-31	Pyrite	b.d.	0.28	45.22	53.04	b.d.	b.d.	b.d.	0.01	98.55
YT-32	Pyrite	0.027	0.08	46.47	53.62	0.01	b.d.	b.d.	b.d.	100.20
YT-32	Pyrite	0.080	b.d.	46.48	53.61	0.01	b.d.	0.02	b.d.	100.19
YT-32	Pyrite	b.d.	0.20	46.22	53.50	b.d.	b.d.	b.d.	0.01	99.92
YT-32	Pyrite	0.069	b.d.	46.01	53.69	b.d.	b.d.	b.d.	b.d.	99.77
YT-41	Pyrite	0.050	0.04	46.02	53.03	b.d.	b.d.	b.d.	0.01	99.16
YT-41	Pyrite	b.d.	0.07	46.23	53.60	b.d.	b.d	b.d.	0.02	99.92
YT-41	Pyrite	0.024	2.38	45.76	51.05	b.d.	0.02	b.d.	0.01	99.25
YT-41	Pyrite	0.050	5.84	44.56	48.71	b.d.	0.01	b.d.	b.d.	99.18
YT-41	Pyrite	0.021	3.91	44.59	51.06	b.d.	b.d.	b.d.	b.d.	99.57
YT-41	Pyrite	0.038	0.17	46.03	53.48	0.01	b.d.	b.d.	b.d.	99.73
YT-42	Pyrite	0.033	0.10	46.08	53.12	b.d.	b.d.	b.d.	b.d.	99.33
YT-42	Pyrite	0.037	3.30	45.48	51.61	b.d.	b.d.	b.d.	b.d.	100.43
YT-42	Pyrite	b.d.	0.05	46.17	53.84	b.d.	b.d.	b.d.	0.03	100.07
YT-42	Pyrite	0.018	4.07	45.70	50.93	b.d.	b.d.	b.d.	0.01	100.73
YT-42	Pyrite	0.027	0.08	46.68	53.55	b.d.	0.01	0.01	b.d.	100.36
YT-42	Pyrite	0.013	0.07	46.80	53.50	b.d.	0.01	0.01	0.02	100.43
YT-43	Pyrite	0.077	b.d.	46.72	53.70	0.01	0.01	0.01	0.01	100.53
YT-43	Pyrite	0.029	4.40	45.30	50.95	b.d.	b.d.	b.d.	0.03	100.71
YT-43	Pyrite	0.025	5.38	44.86	50.09	b.d.	b.d.	b.d.	0.01	100.37
YT-43	Pyrite	b.d.	0.13	46.60	53.69	b.d.	b.d.	b.d.	0.01	100.43
YT-43	Pyrite	b.d.	0.05	46.28	53.53	0.01	b.d.	0.01	b.d.	99.88
YT-43	Pyrite	b.d.	0.07	46.35	53.56	b.d.	b.d.	b.d.	b.d.	99.98
YT-44	Pyrite	0.026	0.05	46.28	53.75	0.01	b.d.	0.01	b.d.	100.14
YT-44	Pyrite	b.d.	0.07	45.88	53.62	0.01	0.01	b.d.	0.03	99.61
YT-44	Pyrite	0.036	0.05	45.75	52.77	b.d.	b.d.	b.d.	b.d.	98.60
YT-44	Pyrite	0.010	0.23	45.80	53.65	0.02	b.d.	b.d.	0.01	99.72
YT-44	Pyrite	0.031	b.d.	45.15	53.47	b.d.	0.01	b.d.	b.d.	98.66
YT-45	Pyrite	0.019	0.12	45.99	52.72	0.01	0.01	b.d.	0.01	98.89
YT-45	Pyrite	0.012	0.18	45.57	52.36	b.d.	0.01	b.d.	0.03	98.17
YT-45	Pyrite	0.043	0.19	45.83	52.86	b.d.	b.d.	b.d.	0.02	98.95
YT-45	Pyrite	b.d.	0.21	45.88	53.55	0.01	0.02	0.01	0.01	99.69
YT-45	Pyrite	0.009	b.d.	46.03	53.37	b.d.	b.d.	b.d.	b.d.	99.44
YT-46	Pyrite	b.d.	b.d.	46.46	53.71	0.03	b.d.	b.d.	b.d.	100.20
YT-46	Pyrite	0.050	0.07	46.29	53.84	0.02	b.d.	b.d.	b.d.	100.26
YT-46	Pyrite	0.018	0.03	46.52	53.71	b.d.	b.d.	0.03	b.d.	100.31
YT-46	Pyrite	b.d.	0.05	46.51	53.89	b.d.	b.d.	b.d.	b.d.	100.45

b.d. = below detection